UNIVERSITY OF LEEDS

This is a repository copy of *The coordinated radio and infrared survey for high-mass star formation - IV. A new radio-selected sample of compact galactic planetary nebulae*.

White Rose Research Online URL for this paper:
http://eprints.whiterose.ac.uk/138669/

Version: Published Version

Article:
Irabor, T, Hoare, MG orcid.org/0000-0003-2684-399X, Oudmaijer, RD et al. (6 more authors) (2018) The coordinated radio and infrared survey for high-mass star formation - IV. A new radio-selected sample of compact galactic planetary nebulae. Monthly Notices of the Royal Astronomical Society, 480 (2). pp. 2423-2448. ISSN 0035-8711

https://doi.org/10.1093/mnras/sty1929

This article has been accepted for publication in Monthly Notices of the Royal Astronomical Society ©: 2018 The Author(s). Published by Oxford University Press on behalf of the Royal Astronomical Society. All rights reserved.

Reuse
Items deposited in White Rose Research Online are protected by copyright, with all rights reserved unless indicated otherwise. They may be downloaded and/or printed for private study, or other acts as permitted by national copyright laws. The publisher or other rights holders may allow further reproduction and re-use of the full text version. This is indicated by the licence information on the White Rose Research Online record for the item.

Takedown
If you consider content in White Rose Research Online to be in breach of UK law, please notify us by emailing eprints@whiterose.ac.uk including the URL of the record and the reason for the withdrawal request.

White Rose university consortium
Universities of Leeds, Sheffield & York

eprints@whiterose.ac.uk
https://eprints.whiterose.ac.uk/

Monthly Notices
of the
ROYAL ASTRONOMICAL SOCIETY

MNRAS **480,** 2423–2448 (2018)
Advance Access publication 2018 July 19

doi:10.1093/mnras/sty1929

The coordinated radio and infrared survey for high-mass star formation – IV. A new radio-selected sample of compact galactic planetary nebulae

T. Irabor,[1⋆] M. G. Hoare,[1⋆] R. D. Oudmaijer,[1] J. S. Urquhart,[2,3] S. Kurtz,[4] S. L. Lumsden,[1] C. R. Purcell,[6] A. A. Zijlstra[5] and G. Umana[7]

[1]*School of Physics & Astronomy, University of Leeds, Leeds LS2 9JT, United Kingdom*
[2]*Centre for Astrophysics and Planetary Science, University of Kent, Canterbury CT2 7NH, UK*
[3]*Max-Planck-Institut für Radioastronomie, Auf dem Hügel 69, D-53121 Bonn, Germany*
[4]*Centro de Radioastronomia y Astrofisica, Universidad Nacional Autonoma de Mexico, 58089 Morelia, Michoacan, Mexico*
[5]*Jodrell Bank Centre for Astrophysics, Alan Turing Building, School of Physics and Astronomy, The University of Manchester, Oxford Road, Manchester, M13 9PL, UK*
[6]*Dept. of Physics and Astronomy, Macquarie University, NSW 2109 Sydney, Australia*
[7]*INAF-Osservatorio Astrofisico di Catania, Via S. Sofia 78, I-95123 Catania, Italy*

Accepted 2018 July 16. Received 2018 July 14; in original form 2018 April 17

ABSTRACT

We present a new radio-selected sample of PNe from the CORNISH survey. This is a radio continuum survey of the inner Galactic plane covering Galactic longitude, $10^\circ < l < 65^\circ$ and latitude, $|b| < 1^\circ$ with a resolution of 1.5 arcsec and sensitivity better than 0.4 mJy beam^{-1}. The radio regime, being unbiased by dust extinction, allows for a more complete sample selection, especially towards the Galactic mid-plane. Visual inspection of the CORNISH data, in combination with data from multiwavelength surveys of the Galactic plane, allowed the CORNISH team to identify 169 candidate PNe. Here, we explore the use of multiwavelength diagnostic plots and analysis to verify and classify the candidate PNe. We present the multiwavelength properties of this new PNe sample. We find 90 new PNe, of which 12 are newly discovered and 78 are newly classified as PNe. A further 47 previously suspected PNe are confirmed as such from the analysis presented here and 24 known PNe are detected. Eight sources are classified as possible PNe or other source types. Our sample includes a young sub-sample, with physical diameters <0.12 pc, brightness temperatures (>1000 K) and located closer than 7 kpc. Within this sample is a water-maser PN with a spectral index of -0.55 ± 0.08, which indicates non-thermal radio emission. Such a radio-selected sample, unaffected by extinction, will be particularly useful to compare with population synthesis models and should contribute to the understanding of the formation and evolution of PNe.

Key words: catalogues – surveys – planetary nebulae: general – stars: evolution – radio continuum: ISM.

1 INTRODUCTION

Planetary nebulae (PNe) are ionized envelopes of dust and gas, ejected during the asymptotic giant branch (AGB) phase of intermediate- mass stars ($0.8\,M_\odot \leq M \leq 8.0\,M_\odot$). These objects (PNe) are known to exhibit simple to complex morphologies (Balick 1987; Sahai et al. 2011). More than 80 per cent of observed PNe show non-spherical morphologies (Parker et al. 2006; Sahai et al. 2007. Also see Kwok 2010), which raises the question of how the deviation from spherical symmetry is achieved, especially with multipolar, point-symmetric, and irregular morphologies. Collimated fast winds or jets have been proposed as the primary shaping agents during the post-AGB phase, where the jet characteristics determine the shape of the PNe when photoionization starts (Sahai & Trauger 1998). The genesis of the collimated jet activities and the driving mechanisms are still not well constrained. Other proposed shaping agents are rotation and/or magnetic fields in single stellar systems (García-Segura et al. 1999, 2005), binary companions, and even triple stellar systems (see De Marco 2009; De Marco et al. 2015; Bear & Soker 2017; and references therein).

Understanding these objects and how they form and evolve is key to understanding the late phase evolution of intermediate-mass stars. Achieving this will require an uncontaminated and representative sample that covers the different stages of their evolutionary

⋆ E-mail: ee11ts@leeds.ac.uk (TI); m.g.hoare@leeds.ac.uk (MGH)

© 2018 The Author(s)
Published by Oxford University Press on behalf of the Royal Astronomical Society

Downloaded from https://academic.oup.com/mnras/article-abstract/480/2/2423/5056229 by University of Leeds user on 14 November 2018

sequence, including very young PNe, where the physical processes associated with shaping and formation may still be active. Zijlstra & Pottasch (1991) predicted the Galactic disc PNe population to be 23 000± 6000. From population synthesis, Moe & De Marco (2006) estimated a total Galactic PNe population of 46 000± 13 000 PNe (with radii < 0.9 pc), assuming single and binary stellar systems result in PNe. About 3540 have been identified so far, including true, likely, and possible PNe (Parker, Bojičić & Frew 2017).

Optical surveys are usually used to search for, and identify these objects from characteristic emission lines associated with their ionized regions. However, the optical regime is limited in various ways, especially in the Galactic plane. Optical surveys are strongly affected by dust extinction, which causes a bias in the sample selection of PNe from such surveys. An optical survey cannot always distinguish very young and compact PNe from other compact, ionized objects such as H II regions (Frew & Parker 2010) and symbiotic systems (Kwok 2003). To overcome dust extinction and incompleteness associated with optical surveys, it is necessary to observe PNe at longer wavelengths.

Samples of PNe themselves are not homogeneous because they possess different morphologies, central star masses, evolutionary stages, ionization characteristics, and different environments. This makes the identification of PNe more challenging. However, to eliminate possible sample contamination by other sources that share similar observational properties and apply a proper constraint on the source classification, there is a need for multiwavelength techniques (Frew & Parker 2010). This is possible because PNe have associated ionized gas, dust emission, and some even have molecular emission (Kwok 2007; Ramos-Larios et al. 2017), making them strong emitters at infrared and radio wavelengths. Infrared surveys can be used to search for PNe that are not visible in the optical because of extinction and free–free emission from their associated ionized gas can be explored at radio wavelengths.

The CORNISH survey provides a high resolution and unbiased radio survey of the northern Galactic plane (Hoare et al. 2012, hereafter Paper I). It covers the northern survey region of the *Spitzer* GLIMPSE I survey (Benjamin et al. 2003; Churchwell et al. 2009). Hence, it provides a complementary radio data and, with its depth and resolution, it is well suited for the search and study of compact PNe. The CORNISH team have visually identified 169 candidate PNe (CORNISH-PNe) from this survey using their appearance at different wavelengths (a combination of the radio, infrared image data, and millimetre dust continuum; see Section 2.2).

The first large scale radio survey that was used to construct a sample of PNe unbiased by extinction is the NRAO VLA sky survey (NVSS) with a resolution of 45 arcsec (Condon et al. 1998). Within the coverage of this survey (full sky survey north of δ-40), 702 of the then known 885 PNe in the Strasbourg-ESO catalogue of Galactic planetary nebulae (Acker et al. 1992) were detected at the time (Condon & Kaplan 1998; Condon, Kaplan & Terzian 1999). With a sensitivity of $\sim$ 2.5 mJy beam^{-1}, this survey was also used to reject contaminants and detect free–free emission towards 454 candidate PNe in the IRAS point source catalogue, 332 of which were known PNe and 122 were identified as candidate PNe (Condon et al. 1999).

In this paper, we examine and analyse the nature of the 169 CORNISH-PNe. We also explore their multiwavelength properties to classify and identify possible contaminants within the sample. Section 2 describes the data and PNe sample selection. The radio properties and use of different multiwavelength diagnostic plots including extinction and distances are presented in Section 3. Discussion of results is presented in Section 4 and the CORNISH-PNe catalogue is described in Section 5.

2 CANDIDATE RADIO PNE SAMPLE

2.1 The CORNISH Survey

The CORNISH survey is a 5 GHz radio continuum survey covering 110 deg^2 of the northern Galactic region, defined by $10^\circ < l < 65^\circ$ and $|b| < 1^\circ$. It probes free-free emission from the ionized regions of compact Galactic sources using the B and B'n'A configurations of the Very Large Array (VLA; Paper I). With its resolution of 1.5 arcsec and sensitivity better than 0.4 mJy beam^{-1}, it forms the radio continuum part of a series of high-resolution, high-sensitivity multiwavelength surveys of the northern Galactic plane. The CORNISH survey provides a combination of higher resolution and depth compared to previous radio surveys of the Galactic plane.

Objects identified in the CORNISH survey include H II regions, PNe, radio galaxies with lobes, and radio stars. The resolution and sensitivity of this survey, together with other comparable surveys of the northern Galactic plane at different wavelengths, is able to discriminate between compact ionized sources. In addition, it should aid identification of new PNe not detected by previous surveys. Details of the survey design, scientific motivation, data reduction, and measurements of properties are provided in Paper I and Purcell et al. 2013 (hereafter Paper II).

2.2 PNe candidate selection

PNe emit at radio and infrared wavelengths due to their associated ionized gas and warm dust. Despite the different morphologies, ionization characteristics, and central star masses, PNe typically appear red and isolated in the infrared. However, they are sometimes confused with HII regions and both can get mixed up in the same sample, depending on the distance and how compact and/or young the H II regions are. This is because H II regions also emit at radio and infrared wavelengths from associated ionized gas and dust.

In the infrared, these two classes of objects can be distinguished by looking at their local environment and morphology. H II regions, unlike PNe, are associated with dense molecular material, which becomes very evident in the MIR as strong PAH (polycyclic aromatic hydrocarbon) emission. This also gives them strong millimetre (mm) dust continuum (Urquhart et al. 2013), whereas PNe are usually very faint or not detected in dust continuum surveys. A comparison of the CORNISH and ATLASGAL survey[1] revealed only a handful of PNe (see Urquhart et al. 2013). H II regions also show regions of strong dust extinction and often form in complexes. PNe, on the other hand, often do not show any form of association with dense molecular material or form in complexes. Furthermore, H II regions often show a variety of irregular morphologies (Wood & Churchwell 1989a) as opposed to PNe whose morphologies usually show a good degree of symmetry (Sahai et al. 2011). This difference in morphology is also clearly seen in MIR images. In the near-infrared (NIR), HII regions are redder than PNe due to the amount of dust emission and sometimes they are not even detected, owing to very high extinction.

The SEDs (spectral energy distribution) of PNe usually peak between 20 and 100 μm. However, some PNe could peak above

[1] http://www3.mpifr-bonn.mpg.de/div/atlasgal/

Downloaded from https://academic.oup.com/mnras/article-abstract/480/2/2423/5056229 by University of Leeds user on 14 November 2018

100 μm (see Urquhart et al. 2013), due to the range of dust temperatures ($30 \gtrsim T_d > 100$ K) in their circumstellar shell (Pottasch et al. 1984; Kwok, Hrivnak & Milone 1986; Villaver, García-Segura & Manchado 2002). H II regions, on the other hand, peak at longer wavelengths of about 70 μm and above because they possess a larger fraction of cooler dust (Wood & Churchwell 1989b; Anderson et al. 2012). This would result in an overlap in the SED of some PNe with H II regions.

Using these observational differences across the different wavelengths over which PNe emit, the CORNISH team, from visual inspection of multiwavelength image data, classified 169 of the detected sources in the CORNISH 7σ catalogue as candidate PNe (CORNISH-PNe). These criteria were also used by Urquhart et al. (2009a) to distinguish between PNe and H II regions in the Red MSX Source survey (Lumsden et al. 2013). The CORNISH-PNe make up ∼ 6per cent of the CORNISH catalogue. The multiwavelength image data used include the Multi-array Galactic Plane Survey (MAGPIS) at 20 cm (White et al. 2005; Helfand et al. 2006), the Galactic Legacy Infrared Mid-Plane Survey Extraordinaire (GLIMPSE; Benjamin et al. 2003; Churchwell et al. 2009), MIPSGAL (Carey et al. 2009), the United Kingdom Infrared Deep Sky Survey (UKIDSS-GPS; Lucas et al. 2008), and the Bolocam Galactic plane survey (BGPS; Rosolowsky et al. 2010a). The use of such multiwavelength data provides a good constraint on the visual classification of compact objects (see Fig. 1), especially towards the Galactic mid-plane, where source crowding is a problem. Observational differences at different wavelengths used by the CORNISH team are illustrated in Fig. 1.

With the visual classification, it is expected that radio stars, radio galaxies, and other extra-galactic sources have been eliminated. However, having done visual classification of these objects, there is a possibility that the sample is still not contaminant free. Possible contaminants are dusty radio stars and HII regions, especially when they are distant and still very young.

2.3 Multiwavelength data

The CORNISH survey provides information at a single frequency (5 GHz), which is not sufficient to determine the nature and discriminate between compact source types in the CORNISH catalogue. To search for CORNISH-PNe counterparts at other wavelengths, we have queried data from other surveys using the CORNISH coordinates (positional accuracy of 0.1 arcsec; see Paper II). Data query and cross-matching is generally limited by coverage and resolution, and so the choice of surveys considered is based on comparable resolution and coverage. We briefly describe below the details of other surveys in the northern Galactic plane that we have used in the analysis presented here.

2.3.1 MAGPIS (20 cm)

The MAGPIS at 20 cm, is a radio continuum survey of the northern Galactic plane, defined by $5^\circ < l < 48\overset{\circ}{.}5$ and $|b| < 0\overset{\circ}{.}8$. Observations were carried out using the VLA with an angular resolution of ∼5 arcsec and rms noise level of ∼0.3 mJy. Details of this survey are given in Helfand et al. (2006). We have queried the >5σ catalogue for CORNISH-PNe counterparts from the compact radio catalogues compiled by White et al. (2005).

2.3.2 GLIMPSE (mid-infrared)

The GLIMPSE, as one of the *Spitzer* legacy science programmes, is a survey of the inner Galaxy in the mid-infrared (MIR). It covers an area of 220 deg^2, defined by longitude $10^\circ < l < 65^\circ$, $-10^\circ > l > -65^\circ$ and latitude $|b| \leq 1^\circ$ with a spatial resolution of ∼2 arcsec. This survey made use of the infrared array camera (IRAC) mounted on the *Spitzer Space Telescope* (*SST*), centred on 3.6, 4.5, 5.8, and 8.0 μm. It achieved a 3σ point source sensitivity of 0.2, 0.2, 0.4, and 0.4 mJy for the four bands, respectively (Benjamin et al. 2003; Churchwell et al. 2009).

2.3.3 UKIDSS (NIR)

The Galactic plane survey (GPS), which is one of the five UKIDSS surveys, covers an area of 1868 deg^2 defined by Galactic latitude $|b| \leq 5^\circ$ and longitude of $15^\circ < l < 107^\circ$, and $142^\circ < l < 230^\circ$ with a seeing of ∼1.0 arcsec. These regions were imaged in the *J*, *H*, and *K* bands centred on 1.25, 1.65, and 2.20 μm, to a depth of 20, 19.1, 19.0 in magnitudes, respectively. Full details of the survey and data release are given in Lucas et al. (2008).

2.3.4 MIPSGAL and WISE (MIR/FIR)

The MIPSGAL is one of the *Spitzer* Galactic plane surveys covering 278 deg^2 of Galactic longitude $5^\circ < l < 63^\circ$ and $298^\circ < l < 355^\circ$ and latitude $|b| < 1^\circ$ regions. This survey was carried out using the MIPS (Multiband Infrared Photometer for *Spitzer*) on the *SST* at 24 and 70 μm, achieving a resolution of 6 and 18 arcsec, respectively. From this survey, we used only the 24 μm data within the $5^\circ < l < 63^\circ$ region with a point source sensitivity at 3σ of 2 mJy (Carey et al. 2009).

The *Wide-field Infrared Survey Explorer* (*WISE*) is an infrared all-sky survey in four bands, centred on 3.4, 4.6, 12, and 22 μm. This survey achieved a 5σ point source sensitivity better than 0.08, 0.11, 1.0, and 6.0 mJy with angular resolutions of 6.1, 6.4, 6.5, and 120 arcsec in the four bands, respectively (Wright et al. 2010). Among other objects, this survey has also uncovered a number of PNe (Ressler et al. 2010; Kronberger et al. 2014). From this survey, we have taken the 12 and 22 μm data to complement the GLIMPSE and MIPSGAL data.

2.3.5 Hi-Gal (far-infrared)

The Hi-Gal (Herschel infrared Galactic Plane Survey) is a far-infrared survey of the Galactic plane, covering $-70^\circ \leq l \leq +68^\circ$; $|b| \leq 1^\circ$ region in five wavebands. This survey used the PACS (Poglitsch et al. 2008) and SPIRE (Griffin et al. 2009) photometric cameras of the Herschel space observatory centred on 70, 160, 250, 350, and 500 μm. It achieved a spatial resolution of 6.0, 12.0, 18.0, 24.0, and 35.0 arcsec in the five bands, respectively. Full details about observation, processing, and data release are given in Molinari et al. (2010, 2016).

2.3.6 IPHAS (H α)

The INT (Isaac Newton Telescope) Photometric H α survey (IPHAS) of the Galactic plane is a 1800 deg^2 CCD survey, covering the Galactic latitude $|b| < 5^\circ$ and longitude $30^\circ < l < 215^\circ$ region, in the broad-bands sloan *r*, *i,* and narrow-band H α filters. The wide field camera (WFC) of the 2.5 m INT with a pixel scale of

Downloaded from https://academic.oup.com/mnras/article-abstract/480/2/2423/5056229 by University of Leeds user on 14 November 2018

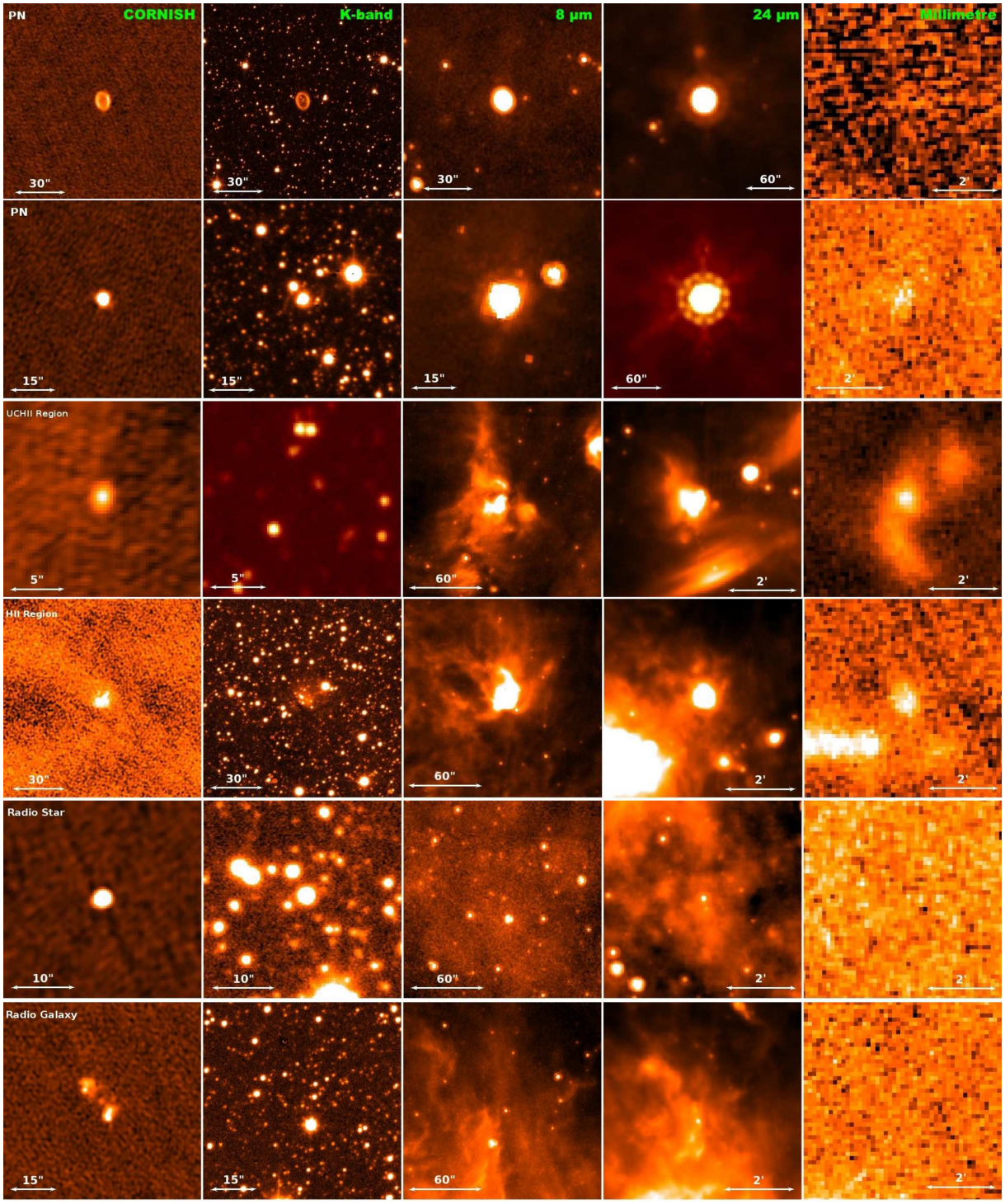

Figure 1. Multiwavelength observational differences between PNe and other sources identified in the CORNISH survey. Surveys from left to right: CORNISH 5 GHz radio, UKIDSS-GPS (*K* band), GLIMPSE (8 μm), MIPSGAL (24 μm), and BGS 1.1 mm dust continuum. The sources from top to bottom are PNe: G051.5095+00.1686 and G035.4719–00.4365; UCH II region: G010.3204–00.2586; HII region: G053.1865+00.2085; Radio star: G045.3657–00.2193 and Radio galaxy: G054.1703–00.0092. These are the main multiwavelength surveys used by the CORNISH team to select the CORNISH-PNe sample.

0.33 arcsec was used for this survey. It is the first fully photometric H α survey of the Galactic plane with mean 5σ depths of 21.2, 20.0, and 20.3 for the *r*, *i*, and H α bands in the Vega magnitude system, respectively (Drew et al. 2005; González-Solares et al. 2008; Barentsen et al. 2014). This survey has a median seeing of ∼1.0 arcsec and has detected both unresolved and resolved PNe, including PNe with lower surface brightness than previously known (Mampaso et al. 2006). Corradi et al. (2008) and G143 have used

Downloaded from https://academic.oup.com/mnras/article-abstract/480/2/2423/5056229 by University of Leeds user on 14 November 2018

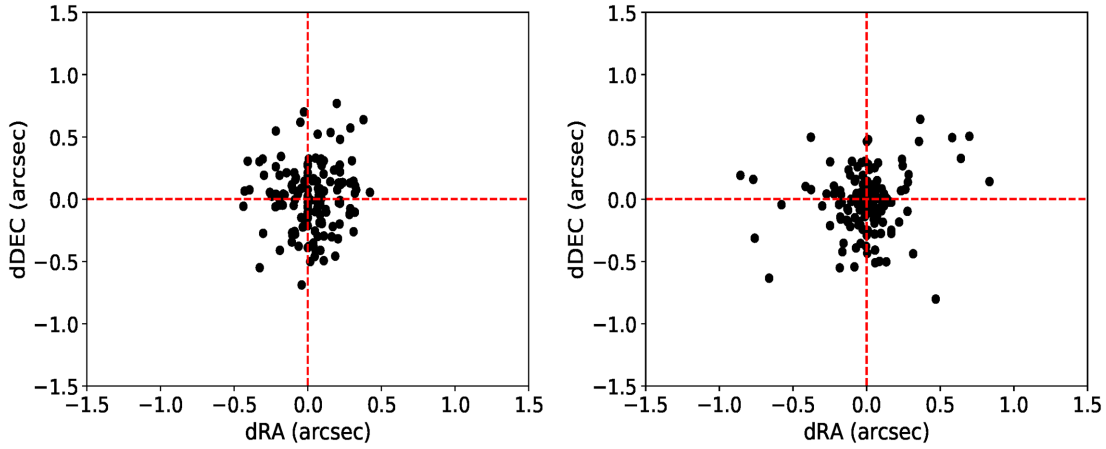

Figure 2. Offset positions in RA and Dec. between the CORNISH-PNe and point source counterparts in the GLIMPSE (left) and UKIDSS (right).

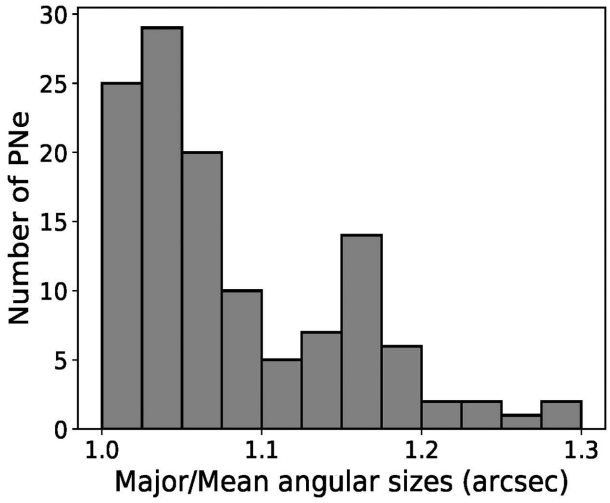

Figure 3. Distribution of the ratios of the major axes to the geometric mean sizes for the CORNISH-PNe.

the $(r - \mathrm{H}\alpha)$ versus $(r - i)$ colour–colour plane in combination with NIR colours to identify and separate PNe from other source classes.

2.4 Aperture photometry

To measure the magnitudes and integrated flux densities of extended sources (absent in published point source catalogues) from some of the surveys, we have performed aperture photometry. This was done using the corresponding CORNISH-PN aperture as a reference. Details on how the fluxes of extended sources in the CORNISH survey were measured are given in Paper II, and we have used the same methods here. In measuring the integrated flux densities of the CORNISH sources, a 2D Gaussian was used for point sources and manually drawn polygons for extended sources.

The MIR emission is expected from a region larger than the ionized gas region due to dust and molecular emissions. This informs the need for a larger aperture for the GLIMPSE data. We define a parameter that allows the size of the reference aperture to be adjusted accordingly by adding an optimal value. The optimal parameter value, which in turn defines an optimal aperture size, was determined from a curve of growth. The need for an optimal aperture was to avoid larger errors due to poor background subtraction (worst for point sources). We have used different apertures for the four bands due to the varying resolution and the varying strength of these emissions across the four bands. We increased the reference apertures by 2.5, 2.5, 3.5, and 4.5 arcsec for the 3.6, 4.5, 5.8, and 8.0 μm, respectively. For the NIR and optical, we have increased the reference aperture size by 1 arcsec.

The background level for each source was measured by means of an annulus, which provides a good estimate of the background level around a source. Due to background variations across the different wavelengths, the median background level was used, since it is not sensitive to extreme values or bright sources in the background. An annulus width of 10 arcsec, with an offset of 5 arcsec from the source aperture was used to estimate the median background level. This ensures that the area of the annulus is greater than the source aperture area, allowing a better estimation of the median background level (Reach et al. 2005). Aperture photometry was performed using equations 19 and 22 in Paper II.

For all data considered, the CORNISH-PNe positions were used to obtain uniform image cut-outs from the latest processed and final calibrated images, where stated or available. Cross-matching of the CORNISH-PNe with individual survey catalogues (UKIDSS and GLIMPSE) was done to compare point source integrated flux densities/magnitudes with results of our aperture photometry. In all cases, the results were similar and showed good agreement for point sources.

This UKIDSS survey has a positional accuracy of ∼0.1 arcsec and the point source catalogue[2] was queried within a 2 arcsec radius. We used the option of nearest objects only to ensure correct matches due to crowded field. The cross-matched positions revealed no systematic offsets (Fig. 2). Aperture photometry was not done for the MAGPIS survey, where we have used the published catalogue values, due to its resolution of ∼6 arcsec compared to the

[2]http://wsa.roe.ac.uk:8080/wsa/crossID_form.jsp

Downloaded from https://academic.oup.com/mnras/article-abstract/480/2/2423/5056229 by University of Leeds user on 14 November 2018

Table 1. The measured radio sizes ($\theta_{\rm FWHM}$), deconvolved sizes ($\theta_{\rm d}$), corrected sizes ($\theta_{\rm true}$) compared to the optical angular sizes ($\theta_{\rm Lit}$) from the MASH (Parker et al. 2006; Miszalski et al. 2008) and IPHAS (Sabin et al. 2014) catalogues are presented. Where available, we show the major and minor optical sizes. Bipolar PNe are indicated with *.

CORNISH name	$\theta_{\rm FWHM}$ (arcsec)	$\theta_{\rm d}$ (arcsec)	$\theta_{\rm true}$ (arcsec)	$\theta_{\rm Lit}$ (arcsec)
G014.5851+00.4613	3.28 ± 0.04	2.91 ± 0.05	4.93 ± 0.08	6.0 × 5.0
G018.2402–00.9152	8.08 ± 0.03	7.94 ± 0.03	12.88 ± 0.05	12.0 × 12.0
G026.8327–00.1516	2.52 ± 0.07	2.03 ± 0.08	3.55 ± 0.15	7.0 × 5.0
G027.6635–00.8267*	1.67 ± 0.06	0.73 ± 0.14	1.38 ± 0.26	35.0 × 12.0
G032.5485–00.4739	2.16 ± 0.04	1.55 ± 0.05	2.78 ± 0.09	9.0 × 9.0
G035.5654–00.4922	6.24 ± 0.03	6.05 ± 0.03	9.88 ± 0.05	11.0 × 11.0
G050.4802+00.7056*	1.60 ± 0.06	0.56 ± 0.16	1.08 ± 0.31	19.0
G051.8341+00.2838	2.25 ± 0.03	1.68 ± 0.05	2.98 ± 0.08	6.0
G062.7551–00.7262*	2.27 ± 0.07	1.71 ± 0.09	3.04 ± 0.16	27.0

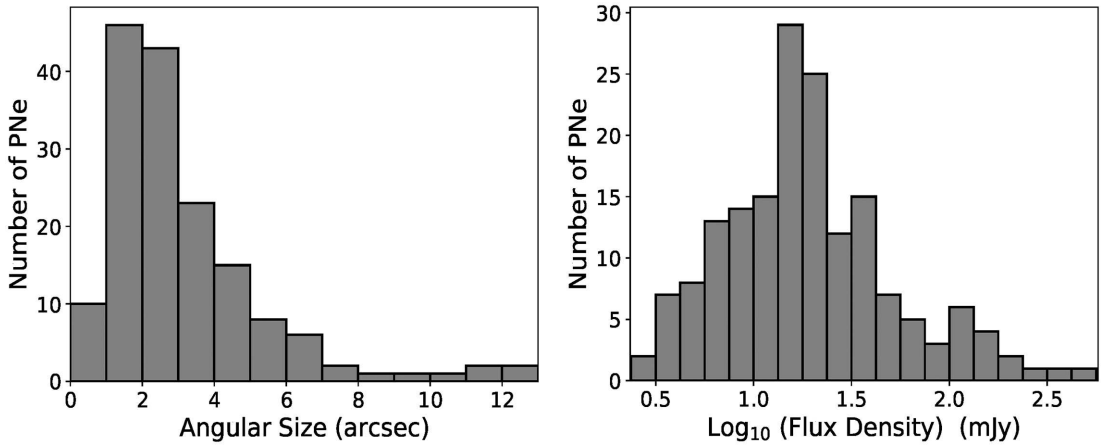

Figure 4. The angular size distribution of the CORNISH-PNe and integrated flux density (right) distribution of the CORNISH-PNe.

CORNISH resolution of 1.5 arcsec. This also applies to the Hi-Gal, MIPSGAL, and *WISE* data.

3 RESULTS AND ANALYSIS

3.1 Radio properties

The primary properties of a radio source are its integrated flux density and angular size. Details of the angular sizes and integrated flux densities measurements of sources in the CORNISH catalogue are given in Paper II and we have briefly summarized it here.

Source detection and photometry was performed using OBIT[3] FndSou. FndSou works by finding and identifying neighbouring islands of emission above a set intensity cut-off and it attempts to fit one or more 2D Gaussians to these emissions. An elliptical aperture was used to measure the source properties, which extended to the 3σ Gaussian major and minor axes. The rms noise and median background level of the sky were measured as described in Section 2.4. For extended sources, indicated by a cluster of Gaussian fits, the fitted parameters were replaced with single measurements under a manually drawn polygon around the emission. For such extended sources, the fitted Gaussian axes are replaced with intensity-weighted diameter given by equation 16 in Paper II.

We have used the geometric mean of the fitted Gaussian axes for point sources ($\sqrt{\theta_{\rm M}\theta_{\rm m}}$, where $\theta_{\rm M}$ and $\theta_{\rm m}$ are the fitted major and minor axes, respectively) and intensity-weighted diameter for extended sources. Because the CORNISH-PNe are fairly round in the radio, there is not much difference between the geometric mean sizes used and major axes as shown in Fig. 3. The intensity weighted sizes would make the extended sources appear smaller than they would in optical catalogues. The deconvolved sizes may also underestimate the sizes of extended sources (see van Hoof 2000). To estimate the true angular sizes, we use a correction factor at 6 cm, according to van Hoof (2000). With this method, $\theta_{\rm true} = \gamma\theta_{\rm d}$ and γ is estimated using equation (1), where $\beta = \theta_{\rm d}/\theta_{\rm beam}$ ($\theta_{\rm d}$ is the deconvolved size):

$$\gamma(\beta) = \frac{0.3429}{1 + 0.7860\beta^2} + 1.6067. \quad (1)$$

Table 1 shows a comparison of the measured sizes (full width at half-maximum, FWHM), deconvolved sizes, calculated true sizes, and reported optical sizes for a few CORNISH-PNe with optical sizes from the MASH[4] (Parker et al. 2006; Miszalski et al. 2008) and IPHAS (Sabin et al. 2014) catalogues. For three of the sources, the optical sizes are 10–20 times larger. These sources are bipolar PNe (G027.6635−00.8267, G050.4802+00.7056, and G062.7551−00.7262) and the CORNISH survey has detected only the bright cores. On the average, the corrected sizes show better agreement with the optical sizes. These corrected angular sizes will be used throughout this paper.

[3] http://www.cv.nrao.edu/~bcotton/Obit.html

[4] Macquarie/AAO/Strasbourg Hα Planetary Galactic Catalogue

Downloaded from https://academic.oup.com/mnras/article-abstract/480/2/2423/5056229 by University of Leeds user on 14 November 2018

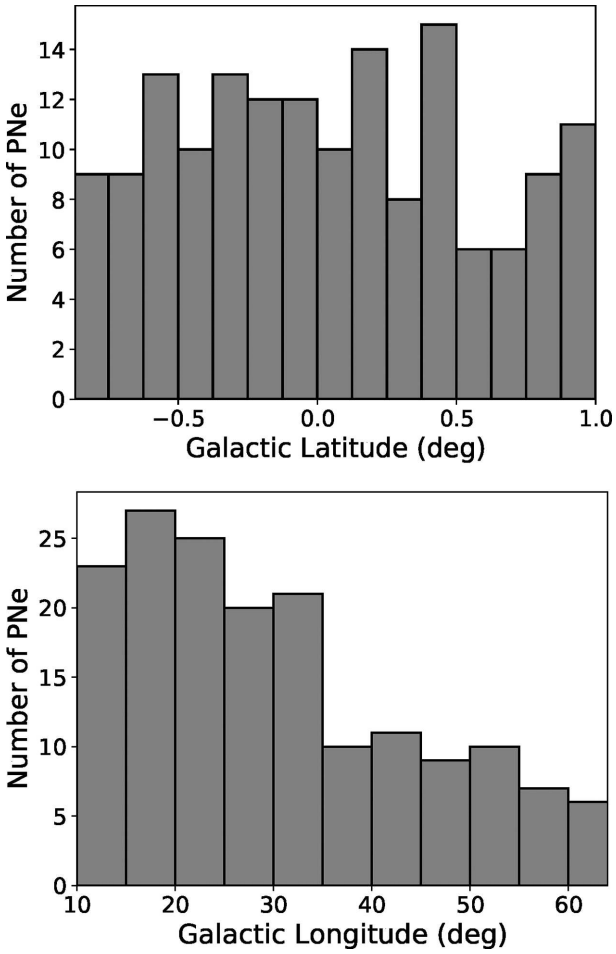

Figure 5. Galactic latitude (upper panel) and longitude (lower panel) distribution of the CORNISH-PNe.

All the CORNISH-PNe have integrated flux density $>7\sigma$, of which 91 per cent are $\leq$100 mJy (Fig. 4, right-hand panel), and $\sim$35per cent are unresolved ($\theta < 1.8$ arcsec). The distribution of the angular sizes with a median of 2.5 arcsec (see left-hand panel in Fig. 4) indicates a preferentially compact and/or distant sample. Fig. 5 (upper panel) shows a Galactic latitude distribution that is approximately flat (upper panel of Fig. 5), indicating a uniform detection of PNe within this region. At such low latitides, we expect detection of PNe from more massive progenitors; hence, a more compact sample of PNe. The longitude distribution (Fig. 5, lower panel) shows an increase in the CORNISH-PNe population towards the Galactic bulge. This agrees with the observed distribution of PNe (see Galactic distribution of known PNe as compiled by Parker et al. 2017[5]), as there are more PNe towards the Galactic centre.

The radio continuum emission from a PN can also be expressed in terms of its brightness temperature (T_b), a distance-independent property that can be used to infer the evolution of PNe. At 6 cm, most PNe are optically thin and so T_b (proportional to the square of the electron density) decreases with continuous expansion as the nebulae evolve. Otherwise, PNe that are optically thick will show high T_b ($T_b = T_e(1 - e^{-\tau_\nu})$, where T_e is the electron temperature), as the optical depth approaches the optically thick limit ($\tau_\nu \propto n_e^2$). Therefore, more evolved and optically thin PNe should have lower brightness temperatures compared to younger and more compact PNe. None the less, young PNe from low-mass progenitors could also show low T_b because the envelope may have been mostly dispersed before the central star becomes hot enough to initiate ionization:

$$T_b = \frac{\lambda^2 S_\nu}{2k\pi\theta^2}. \quad (2)$$

The average T_b across each CORNISH-PNe at 5 GHz was estimated using equation (2), where θ is the angular radius (arcsec) and S_ν is the integrated flux density (mJy). The CORNISH-PNe show T_b between 20 and 7000 K (Fig. 6, left-hand panel) with a median of $\sim$200 K. We also show the variation of the angular sizes with corresponding flux densities and lines of constant T_b in Fig. 6 (right-hand panel). It can be seen that there are a few PNe that can be considered younger. These younger CORNISH-PNe have small angular sizes and T_b that lie within the region of 10^3 K $< T_b < 10^4$ K (see Kwok 1985).

3.1.1 *Spectral Index*

Having shown the possible existence of some young CORNISH-PNe in Fig. 6, it is also important to determine the nature of their radio emission. We cross-matched the CORNISH survey at 6 cm with the MAGPIS radio survey at 20 cm within a radius of 5 arcsec. This resulted in a total of 67 matches out of the 169 CORNISH-PNe. 85 per cent of the cross-matched sources have angular separations less than 1 arcsec and a distribution that peaks about 0.5 arcsec (see Fig. 7).

For the purpose of spectral indices estimation, there is a need to exclude very extended sources, whose emission could have been spatially filtered out due to the design of the CORNISH survey. Spatially filtered out emission will result in underestimated flux densities. To exclude such extended PNe, we compared the CORNISH-PNe integrated flux densities to their corresponding peak fluxes. Sources with angular sizes larger than 9 arcsec, corresponding to $F_{int}/F_{peak} > 10$ were considered too extended. Additionally, the flux densities and angular sizes of the CORNISH-PNe were compared with their counterparts in the 6 cm MAGPIS catalogue (at a lower resolution of 6 arcsec; White et al. 2005). This reduced our sample to 61, after excluding 6 sources considered to be very extended.

To get a more complete sample, we measured the flux densities of the CORNISH-PNe absent from the MAGPIS catalogue as described in Section 2.4, using the CORNISH-PNe positions on the MAGPIS 20 cm image data. This brought our sample to a total of 127 out of 169 PNe. Measured 20 cm flux densities are given in Table 2. The spectral indices and associated errors of the 127 CORNISH-PNe were estimated using equations (3) and (4), where S_1 and S_2 are the flux densities in mJy, and ν_1 and ν_2 are the corresponding frequencies:

$$\alpha = \frac{\ln(S_1/S_2)}{\ln(\nu_1/\nu_2)}, \quad (3)$$

$$\delta\alpha = \frac{1}{\ln(\nu_1/\nu_2)}\sqrt{\left(\frac{\delta S_1}{S_1}\right)^2 + \left(\frac{\delta S_2}{S_2}\right)^2}. \quad (4)$$

Assuming the radio-continuum emission from a PN is free–free, the spectral index range is expected to be between -0.1 and 2, where it is optically thin and optically thick, respectively. Fig. 8 (top panel) shows the distribution of the CORNISH-PNe with a peak at about 0.1, which agrees with optically thin free–free emission.

[5] http://hashpn.space/

Downloaded from https://academic.oup.com/mnras/article-abstract/480/2/2423/5056229 by University of Leeds user on 14 November 2018

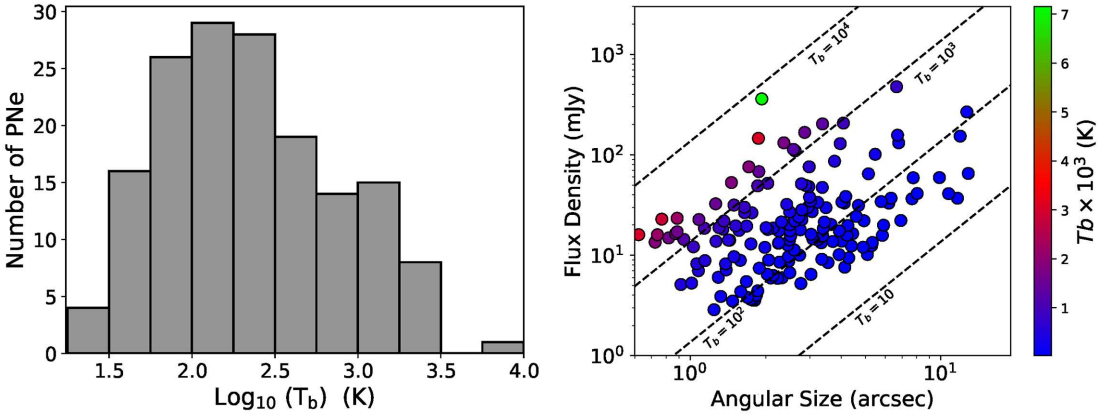

Figure 6. Left-hand panel: brightness temperature distribution. Right-hand panel: brightness temperature versus and angular sizes, showing lines of constant temperature.

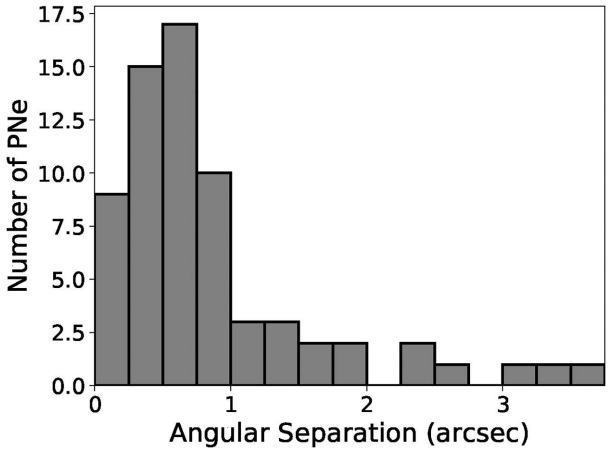

Figure 7. Distribution of the angular separation of the 67 CORNISH-PNe found in the MAGPIS survey within a cross-matching radius of 5 arcsec.

In Fig. 8 (middle panel), ∼84 per cent of the 127 CORNISH-PNe have spectral indices within the theoretical range. However, only two PNe have spectral indices below −0.1 at a 3σ significance level, which is indicative of non-thermal emission (discussed in Section 4.3). These are marked as B (G030.2335–00.1385) and C (G019.2356+00.4951) in Fig. 8 (middle), where we plot spectral index against the log of the CORNISH angular sizes. The source marked A (G052.1498–00.3758) has a spectral index of −0.1 at a 3σ significance level and so its emission is treated as thermal.

If we assume the integrated flux density at 1.4 and 5 GHz are from the same solid angle, we can model the spectral index (1.4 and 5 GHz) at constant electron temperatures of $T_e = 0.5 \times 10^4$, 1.0×10^4, and 1.5×10^4 K as in Siódmiak & Tylenda (2001, see their equations 2 and 5). Results are shown in Fig. 8 (lower panel), where we plot modelled spectral indexes against brightness temperatures at 5 GHz over our data. At 5 GHz, the CORNISH-PNe generally show a scatter around the theoretical, optically thin region of the model. Above T_b= 1000 K, the CORNISH-PNe follow the trend of the model, as spectral index increases with T_b (excluding two outliers). There are a few PNe that approach the optically thick limit with increasing T_b. This trend is also observed in Fig. 8 (middle panel) and Fig. 6 (right-hand panel), where CORNISH-PNe with smaller angular sizes show higher T_b and spectral indices. The observed radio emission of the outliers, marked A (G052.1498–00.3758) and B (G030.2335–00.1385), obviously cannot be explained by a simple model characterized by varying optical depth and constant electron temperature (see Siódmiak & Tylenda 2001). G019.2356+00.4951, G030.2335–00.1385, and G052.1498–00.3758 are further discussed in Sections 4.2 and 4.3. Table 2 summarizes the radio properties of the CORNISH-PNe.

3.2 MIR to radio continuum ratio

It is expected that as the PN evolves with an increase in size, the ratio of the MIR to radio integrated flux density (MIR/radio) will decrease. This is a result of the increased ionized volume as compared to the amount of dust and excited polycyclic aromatic hydrocarbon (PAH) emission, present in the 8.0 μm band. PAH emission in this band arises from the excited PAH molecules just outside the ionized regions of carbon-rich PNe (Cox et al. 2016). As the ionization front spreads out, the PAH emission decreases (Cohen et al. 2007a; Cerrigone et al. 2009; Guzman-Ramirez et al. 2014), causing a decrease in the total flux in the 8 μm band. Thus, compared to more-evolved PNe, younger PNe should have stronger PAH emission, resulting in higher values of the MIR/radio ratio. This ratio can also be affected by the mass-loss history in the AGB phase. However, irrespective of larger angular sizes as a result of evolution, bipolar PNe have high MIR/radio values due to the larger amount of dust and the presence of a torus that could remain molecular for a longer time (Guzman-Ramirez et al. 2014; Cox et al. 2016).

Cohen et al. (2007b, 2011) used this ratio (MIR/radio) to discriminate between PNe and H II regions. H II regions are brighter in the MIR compared to PNe due to the larger amount of molecular gas associated with them. Cohen et al. (2011) reported a median of 4.7 ± 1.1 for the MASH PNe sample using $F_{8.0\,\mu m}/F_{0.843\,GHz}$. For the CORNISH-PNe, we have used the integrated flux densities from the IRAC 8 μm band and the CORNISH survey ($F_{8.0\,\mu m}/F_{5\,GHz}$). The distribution is shown in Fig. 9 with a median of 3.3 ± 1.0. If we convert the 5 GHz flux densities to 0.843 GHz, assuming the CORNISH-PNe are all optically thin, we have a median of 3.3 ± 0.70 (stated error is the standard error on the median). These estimates show a reasonable agreement within 1σ of the Cohen et al. (2011) value. Using the same method, Filipović et al. (2009) found a median value of 9.0 ± 2.0 ($F_{8.0\,\mu m}/F_{1.4\,GHz}$) for 14 Magellanic cloud PNe, which is consistent with our value and Cohen et al. (2011) within 2σ. For the CORNISH-PNe, there is no obvious trend or variation of the $F_{8.0\,\mu m}/F_{5\,GHz}$ with angular sizes.

Downloaded from https://academic.oup.com/mnras/article-abstract/480/2/2423/5056229 by University of Leeds user on 14 November 2018

Table 2. Radio properties of the CORNISH-PNe. For the angular sizes of sources whose deconvolved sizes could not be determined, we propagated an upper limit of 3σ and they are preceded by '<'. Column 8 shows measured (aperture photometry) 1.4 GHz integrated flux densities (MAGPIS) not present in the point source catalogue. Full table is available online as Table A1.

CORNISH Name	RA (J2000)	Dec. (J2000)	$F_{5\,\mathrm{GHz}}$ (mJy)	$F_{1.4\,\mathrm{GHz}}$ (mJy)	Angular size (arcsec)	T_b (K)	Spectral Index
G009.9702–00.5292	18:09:40.54	−20:34:21.7	12.6 ± 1.6	11.55 ± 0.65	2.45 ± 0.25	154.0 ± 29.0	0.07 ± 0.11
G010.0989+00.7393	18:05:13.13	−19:50:35.2	476.0 ± 43.6	–	6.66 ± 0.01	784.0 ± 72.0	0.20 ± 0.07
G010.4168+00.9356	18:05:09.17	−19:28:11.3	14.4 ± 1.5	–	0.94 ± 0.27	1182.0 ± 489.0	–
G010.5960–00.8733	18:12:14.95	−20:11:24.7	34.5 ± 3.8	–	3.02 ± 0.05	276.0 ± 31.0	0.01 ± 0.09
G011.3266–00.3718	18:11:52.34	−19:18:31.0	13.8 ± 2.4	11.63 ± 0.84	4.02 ± 0.11	62.0 ± 11.0	0.14 ± 0.15
G011.4290–01.0091	18:14:27.14	−19:31:26.8	14.6 ± 2.0	–	3.08 ± 0.31	112.0 ± 22.0	−0.40 ± 0.14
G011.4581+01.0736	18:06:47.64	−18:29:37.7	7.4 ± 1.2	–	1.89 ± 0.37	152.0 ± 48.0	–
G011.7210–00.4916	18:13:07.15	−19:01:12.4	5.9 ± 1.1	8.06 ± 0.48	2.10 ± 0.48	98.0 ± 37.0	−0.24 ± 0.16
G011.7434–00.6502	18:13:45.22	−19:04:35.4	156.9 ± 15.0	–	6.72 ± 0.01	253.0 ± 24.0	0.00 ± 0.09
G011.7900–00.1022	18:11:48.89	−18:46:21.4	41.2 ± 6.9	49.10 ± 1.13	8.05 ± 0.08	46.0 ± 8.0	−0.14 ± 0.13

3.3 Multiwavelength colours

The strength of multiwavelength colour–colour diagrams to distinguish between PNe and their contaminants, in the absence of optical data, has been explored by Cohen et al. (2011) and Parker et al. (2012). Such plots allow separation of sources according to their colours. We have placed the CORNISH-PNe on different colour–colour plots and, where necessary, we have compared them with other Galactic sources that could contaminate our sample.

3.3.1 NIR colours

The measured emission of PNe in the J, H, and K bands is a combination of emission from the ionized nebulae, including free-bound and free–free emission, hot dust emission, stellar continuum from the central star, and emission lines. The ionized gas and hot dust should dominate the emission, but in some cases, the stellar continuum could be mostly responsible (Whitelock 1985; Garcia-Lario et al. 1997; Ramos-Larios & Phillips 2005; Phillips & Zepeda-Garcia 2009).

Fig. 10 shows the distribution of the CORNISH-PNe on the $J - H$ versus $H - K$ colour–colour plane (measured magnitudes are presented in Table 5). We also show the position of symbiotic stars, the intrinsic colours of an O9 star from Ducati et al. (2001) and the modelled intrinsic colours of NGC 7027 (0.21, 0.41) and NGC 6720 (0.62, 0.0) from Weidmann et al. (2013). Some of the CORNISH-PNe show colours that are typical of symbiotic stars. This will make it difficult to rely soley on the NIR colour–colour plane in differentiating between PNe and symbiotic stars. The CORNISH-PNe show a broad distribution that can be mostly explained by the range of PNe intrinsic colours (see Ramos-Larios & Phillips 2005; Phillips & Zepeda-Garcia 2009) and differing amounts of extinction.

Categorically, younger PNe with hot dust have redder colours, resulting in higher $H - K$ values. A contribution to the K band could also arise from H_2 emission believed to be excited mainly by shocks and, in some cases, ultra-violet fluorescence (Marquez-Lugo et al. 2015). The presence of this emission in the K band could also lead to an increase in the $H - K$ colour. The colour distribution of the CORNISH-PNe is similar to the IPHAS-PNe, but with more CORNISH-PNe displaying a higher reddening. Compared to the MASH sample analysed by Phillips & Zepeda-Garcia (2009) and PNe from the VVV (VISTA Variables in the Via Lactea) survey by Weidmann et al. (2013), the CORNISH-PNe show a higher reddening. The median colours of the CORNISH-PNe are 1.23 ± 0.05 and 1.25 ± 0.07 for $H - K$ and $J - H$, respectively.

3.3.2 Optical colours

CORNISH-PNe counterparts were searched for within the region of the IPHAS survey that overlaps with the CORNISH survey, using the CORNISH positions. Owing to the Galactic position of these PNe, confusion with other sources in the background or foreground is possible. For this reason, the H α images were visually checked, aided with false three-colour images. None of the images showed complexes or diffuse emission associated with HII regions. A total of 22 out of the 76 CORNISH-PNe within the IPHAS survey region were found to have genuine counterparts. These include extended PNe not present in the point source catalogue. We measured the H α, r, and i magnitudes as discussed in Section 2.4 and measurements are presented in Table 3.

PNe are known to be good emitters of H α, so they can be easily identified on the $[r - \mathrm{H}\ \alpha]$ versus $[r - i]$ colour–colour plane, where normal PNe have large $r - \mathrm{H}\ \alpha$ colours. The positions of PNe in the optical colour–colour plane are well discussed in Corradi et al. (2008) and G143 using PNe from the IPHAS survey. PNe with H α excesses should be located within the upper region of the plot, while reddened PNe should be located towards the right, where higher $[r - i]$ values occur. We also show the positions of some Galactic PNe from the IPHAS survey and symbiotic stars in Fig. 11. This is to show the distribution of the CORNISH-PNe within other PNe samples and possible contaminants like the symbiotic systems that are visible in the optical.

Out of the 22 CORNISH-PNe with IPHAS counterparts, 21 seem to have normal PNe colours (Fig. 11). An exception to this is the colour of G035.4719–00.4365 ($[r - i] \sim 0.92$, $[r - H\,\alpha] \sim 0.69$), where foreground stars in its photometry could be responsible. The general distribution of the CORNISH-PNe does not look different from the IPHAS-PNe. Again, the CORNISH-PNe show colours similar to symbiotic stars and it will be difficult to separate PNe from such contaminants based on this optical colour–colour plots.

3.3.3 Mid-infrared (MIR) colour

The emission of a PN in the MIR is a summation of dust continuum, free–free, free-bound, atomic line, molecular line, and PAH emissions. All these contribute to the colour of a PN and its position on the MIR colour–colour plot, depending on which is dominant.

Downloaded from https://academic.oup.com/mnras/article-abstract/480/2/2423/5056229 by University of Leeds user on 14 November 2018

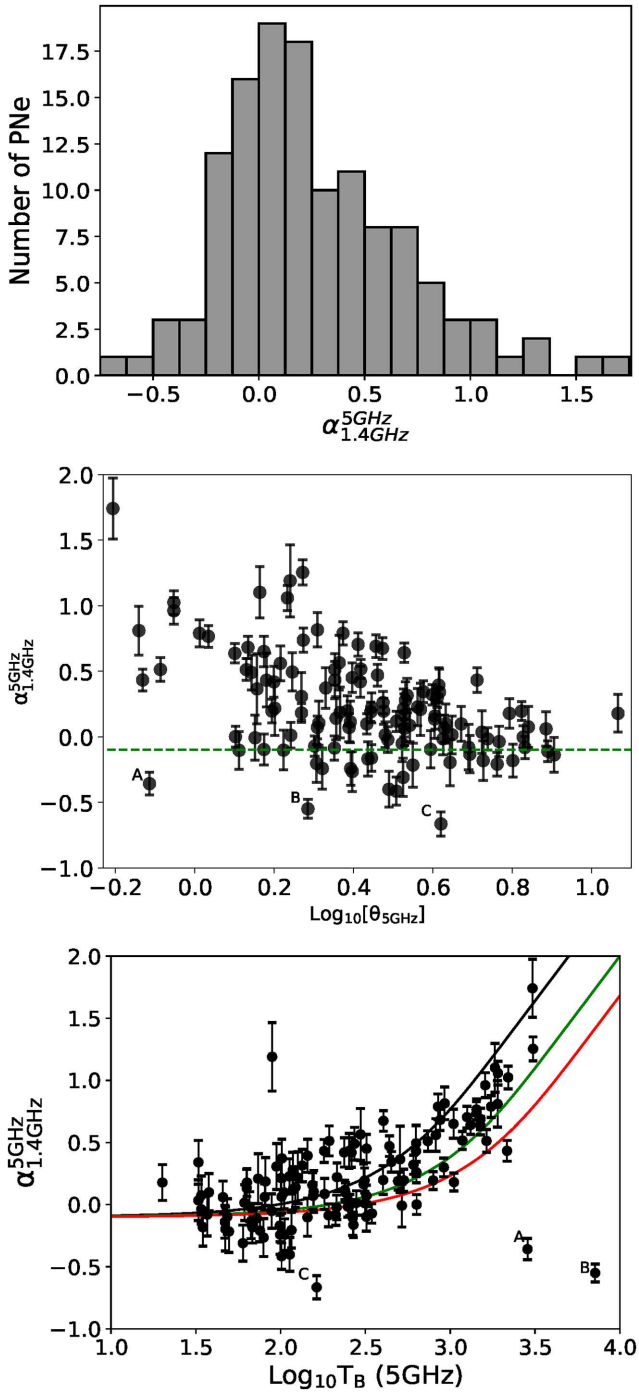

Figure 8. Top: spectral index distribution of the CORNISH-PNe. Middle: distribution of the spectral indices versus the log of the angular sizes. The red filled circles are the PNe with non-thermal emission at a 3σ significance level. Bottom: shows our data overlaid on a model of spectral index (5 GHz to 1.4 GHz) against the brightness temperature at 5 GHz. The curves show predictions of the model for T_e at 0.5×10^4 K (black), 1.0×10^4 K (green), and 1.5×10^4 K (red). The observed radio emission of the outliers, marked A (G052.1498–00.3758), B (G030.2335–00.1385), and C (G019.2356+00.4951), cannot be explained by a simple model characterized by constant electron temperature and varying optical depth (see Siódmiak & Tylenda 2001) (A colour version of this figure is available in the online journal).

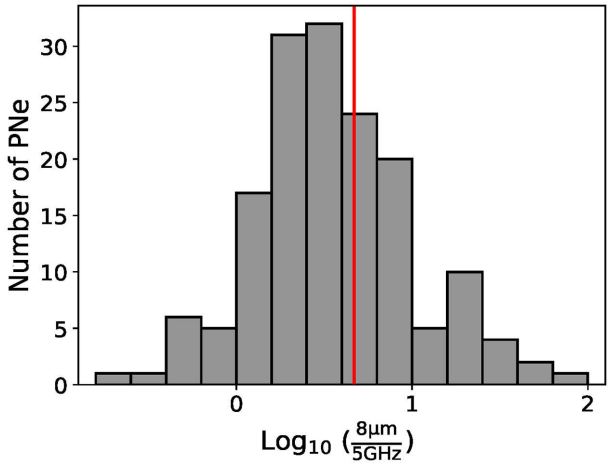

Figure 9. Distribution of the $F_{8.0\,\mu m}/F_{5\,GHz}$ showing the median (red dotted line) from Cohen et al. 2011 (A colour version of this figure is available in the online journal).

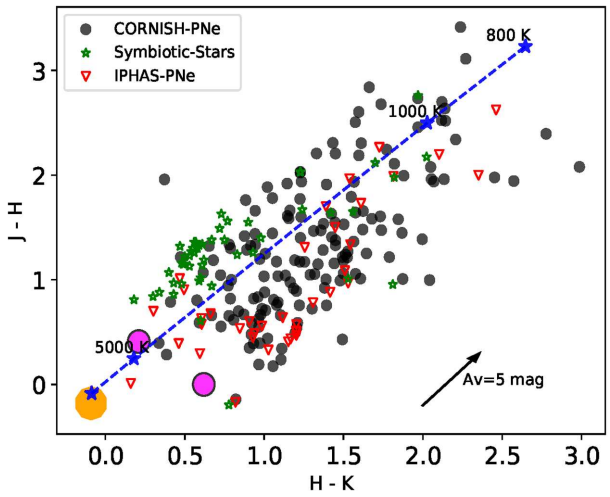

Figure 10. $J - H$ versus $H - K$ colour–colour plot. We have taken PNe sample from the IPHAS catalogue (G143 G142; Sabin et al. 2014); symbiotic stars samples were taken from Corradi et al. (2008, 2010), Rodríguez-Flores et al. (2014), and new symbiotic stars from Miszalski et al. 2013). Modelled intrinsic colours of PNe (NGC 6720 and NGC 7027) shown in magenta (circles) are from Weidmann et al. (2013). We also show the intrinsic colour of an O9 star (orange) from Ducati et al. (2001) and blackbodies at different temperatures (A colour version of this figure is available in the online journal).

The work of Cohen et al. (2011), using the GLIMPSE data, showed that PNe can be well separated from H II regions, using their MIR colours. Cohen et al. (2011) further showed that PNe have distinctive median colour indices compared to H II regions.

In Table 4, we compare median MIR colours of the CORNISH-PNe with the median colours of the MASH-PNe sample analysed by Cohen et al. (2011). The CORNISH-PNe median colours show good agreement within 2σ. Furthermore, we show the colour distribution of the CORNISH-PNe on the [3.6]–[4.5] versus [5.8]–[8.0] and [3.6]–[5.8] versus [4.5]–[8.0] colour–colour planes in Fig. 12. Fig. 12 also shows the positions of PNe sample taken from Cohen et al. (2011), positions of the central stars of PNe (Hora et al. 2004), symbiotic stars (Corradi et al. 2008; Miszalski et al. 2013), the mean colour of UCH II regions sample from the CORNISH

Downloaded from https://academic.oup.com/mnras/article-abstract/480/2/2423/5056229 by University of Leeds user on 14 November 2018

Table 3. H α, r, and i magnitudes and the H α line flux (erg cm^{-2} s^{-1}) for the 22 CORNISH-PNe present in the IPHAS survey. These were measured using aperture photometry as discussed in Section 2.4.

CORNISH name	H α (mag)	r (mag)	i (mag)	LogF($H\alpha$) (erg cm^{-2} s^{-1})
G029.5780–00.2686	16.43 ± 0.01	19.44 ± 0.05	18.78 ± 0.15	− 13.38 ± 0.04
G032.5485–00.4739	13.76 ± 0.01	16.68 ± 0.01	16.12 ± 0.02	− 12.32 ± 0.01
G032.6136+00.7971	19.25 ± 0.11	21.11 ± 0.27	18.26 ± 0.08	− 14.51 ± 0.40
G033.4543–00.6149	16.30 ± 0.01	18.13 ± 0.02	16.75 ± 0.02	− 13.33 ± 0.05
G035.4719–00.4365	14.38 ± 0.01	15.08 ± 0.01	14.15 ± 0.01	− 12.57 ± 0.01
G041.3540+00.5390	18.08 ± 0.12	20.19 ± 0.30	16.82 ± 0.04	− 14.05 ± 0.50
G044.6375+00.4827	16.32 ± 0.01	19.09 ± 0.07	17.27 ± 0.05	− 13.34 ± 0.05
G048.5619+00.9029	16.87 ± 0.03	18.42 ± 0.05	17.71 ± 0.09	− 13.56 ± 0.10
G048.7319+00.9305	15.63 ± 0.01	18.24 ± 0.05	18.05 ± 0.12	− 13.06 ± 0.04
G050.0405+01.0961	16.42 ± 0.02	18.39 ± 0.06	17.33 ± 0.08	− 13.38 ± 0.09
G050.4802+00.7056	16.57 ± 0.01	18.77 ± 0.03	17.69 ± 0.06	− 13.44 ± 0.05[a]
G050.5556+00.0448	17.29 ± 0.03	19.35 ± 0.08	18.23 ± 0.11	− 13.73 ± 0.10
G051.8341+00.2838	16.17 ± 0.01	19.10 ± 0.05	18.15 ± 0.08	− 13.28 ± 0.04
G055.5070–00.5579	10.12 ± 0.01	13.12 ± 0.01	13.35 ± 0.01	− 10.86 ± 0.01
G056.4016–00.9033	14.34 ± 0.01	16.75 ± 0.01	16.13 ± 0.01	− 12.55 ± 0.01
G058.6410+00.9196	18.02 ± 0.06	20.33 ± 0.18	18.57 ± 0.09	− 14.02 ± 0.20
G059.3987–00.7880	15.83 ± 0.01	17.18 ± 0.01	16.02 ± 0.01	− 13.15 ± 0.02
G059.8236–00.5361	14.90 ± 0.01	17.81 ± 0.03	17.29 ± 0.03	− 12.77 ± 0.01
G060.9866–00.5698	14.76 ± 0.01	17.37 ± 0.01	16.79 ± 0.02	− 12.71 ± 0.01
G062.4936–00.2699	11.68 ± 0.01	14.78 ± 0.01	16.46 ± 0.02	− 11.48 ± 0.01
G062.7551–00.7262	14.10 ± 0.01	17.18 ± 0.01	18.46 ± 0.16	− 12.45 ± 0.01[a]
G063.8893+00.1229	13.79 ± 0.01	16.40 ± 0.01	15.92 ± 0.02	− 12.33 ± 0.01[a]

[a]Indicates PNe that are bipolar in the optical.

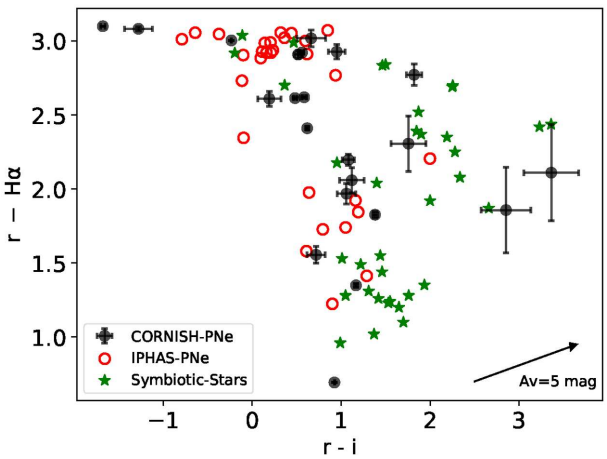

Figure 11. r − H α versus r − i colour–colour plane. We show PNe sample from the IPHAS catalogue (Viironen et al. G143,b; Sabin et al. 2014); symbiotic stars samples from Corradi et al. (2008, 2010) and Rodríguez-Flores et al. (2014), and new symbiotic stars from Miszalski et al. (2013). The reddening vector is from the relationship in Cardelli, Clayton & Mathis (1989) (A colour version of this figure is available in the online journal).

Table 4. Comparison of the median colours of 160 CORNISH-PNe with PNe samples from Cohen et al. (2011).

Colour Index	Cohen et al. (2011) 107	CORNISH-PNe 160
[3.6]–[4.5]	0.81 ± 0.08	0.84 ± 0.08
[3.6]–[5.8]	1.73 ± 0.10	1.94 ± 0.19
[3.6]–[8.0]	3.70 ± 0.11	3.83 ± 0.37
[4.5]–[5.8]	0.86 ± 0.10	1.08 ± 0.11
[4.5]–[8.0]	2.56 ± 0.11	3.01 ± 0.30
[5.8]–[8.0]	1.86 ± 0.07	1.84 ± 0.18

survey (Kalcheva et al. 2018, hereafter Paper III) and the position of blackbodies at different temperatures.

The CORNISH-PNe show the same broad distribution shown by the Cohen et al. (2011) PNe sample and they are well separated from the S-type symbiotic stars and central stars of PNe, which was not seen in Figs 10 and 11 (NIR and optical colour–colour plane). On the [3.6]–[4.5] versus [5.8]–[8.0] plane, the colours of the CORNISH-PNe, dusty (D-type) stars, and UCH II regions seem inseparable. This looks different on the [3.6]–[5.8] versus [4.5]–[8.0] plane, where the CORNISH-PNe seem separated from the mean colour of the CORNISH UCH II regions. This could be as a result of the PAH emission strength in the 8 μm band, compared to bands 3 and 4 μm.

Generally, this broad distribution could be a result of different dominant emission mechanisms across the bands (Phillips & Ramos-Larios 2009). A combination of the evolutionary state and PAH strength across the different bands for carbon rich PNe could also contribute to the wide spread of the CORNISH-PNe colours. Most of the CORNISH-PNe show the red colours typical of PNe, including the ones dominated by dust continuum, H_2, and PAH emission. However, there are a few to the left in Fig. 12 (both colour–colour planes), where stellar continuum could be contributing to their emission. The colours of such PNe could also be a result of dominant ionized gas emission with little or no dust emission. The measured mid-infrared integrated flux densities using aperture photometry are given in Table 5.

3.3.4 FIR colours

The dust content in the circumstellar envelopes of PNe can be better viewed in the FIR, especially when combined with MIR data. This dust, lost during the AGB phase, has temperatures in the range of $\sim 10 \leq T_d \leq 100$ K (Villaver et al. 2002; Van de Steene et al. 2015; Van de Steene 2017).

Downloaded from https://academic.oup.com/mnras/article-abstract/480/2/2423/5056229 by University of Leeds user on 14 November 2018

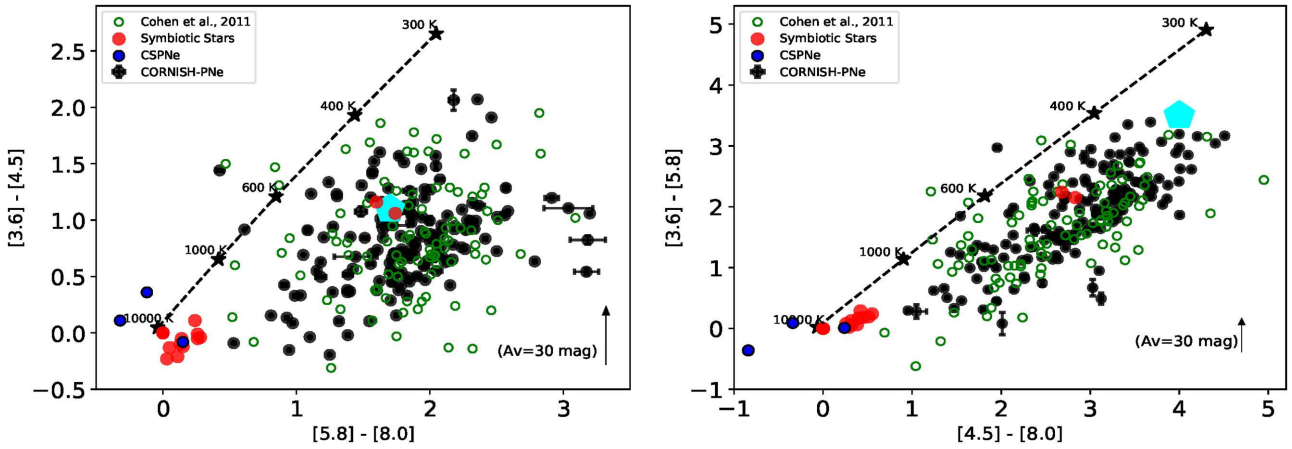

Figure 12. Left-hand panel: [3.6]–[4.5] versus [5.8]–[8.0]. Right-hand panel: [3.6]–[5.8] versus [4.5]–[8.0]. The green circles are PNe (GLIMPSE data) taken from Cohen et al. (2011), blue filled circles are CSPNe (central stars of PNe) taken from Hora et al. (2004) and symbiotic stars from Corradi et al. (2008) and Miszalski et al. (2013) are represented as red filled circles. The cyan hexagon shows the mean colours of UCH IIs from the CORNISH survey (Paper III). We also show blackbodies at different temperatures. The reddening vector is from the average extinction in Indebetouw et al. (2005) (A colour version of this figure is available in the online journal).

Table 5. Measured NIR magnitudes and MIR flux densities for the CORNISH-PNe. These are measured using aperture photometry as described in Section 2.4. In the NIR, some of the CORNISH-PNe were not detected in one or more bands. For such sources,the corresponding columns are left blank. For non-detections in one or more of the bands and where the measured integrated flux density is less than 3σ in the MIR, we have defined an upperlimit of 3σ limit preceded by '<'. Full table is available online as Table A2.

CORNISH name	J (mag)	H (mag)	K (mag)	$F_{3.6}$ (mJy)	$F_{4.5}$ (mJy)	$F_{5.8}$ (mJy)	$F_{8.0}$ (mJy)
G009.9702–00.5292	16.35 ± 0.03	14.69 ± 0.02	13.07 ± 0.02	8.6 ± 0.18	10.15 ± 0.14	15.32 ± 0.22	41.53 ± 0.47
G010.0989+00.7393	10.66 ± 0.02	10.27 ± 0.03	9.34 ± 0.03	228.81 ± 0.18	621.73 ± 0.16	1105.25 ± 0.43	4046.75 ± 0.82
G010.4168+00.9356	14.18 ± 0.02	13.51 ± 0.03	12.64 ± 0.03	8.06 ± 0.09	9.25 ± 0.07	7.9 ± 0.16	57.35 ± 0.16
G010.5960–00.8733	16.16 ± 0.03	14.05 ± 0.01	12.23 ± 0.04	48.09 ± 0.09	46.99 ± 0.07	98.96 ± 0.21	245.86 ± 0.30
G011.3266–00.3718	16.58 ± 0.03	14.27 ± 0.01	12.84 ± 0.01	12.44 ± 0.12	13.22 ± 0.09	20.91 ± 0.23	33.71 ± 0.34
G011.4290–01.0091	11.32 ± 0.01	11.46 ± 0.02	10.64 ± 0.01	27.49 ± 0.11	23.82 ± 0.08	14.76 ± 0.24	20.47 ± 0.32
G011.4581+01.0736	15.56 ± 0.02	14.12 ± 0.01	13.18 ± 0.01	<0.15	9.46 ± 0.08	<0.48	47.58 ± 0.21
G011.7210–00.4916	–	–	–	<0.3	0.91 ± 0.09	<0.63	<1.08
G011.7434–00.6502	10.96 ± 0.01	10.78 ± 0.01	9.73 ± 0.01	157.13 ± 0.18	175.46 ± 0.15	536.58 ± 0.34	1814.38 ± 0.58
G011.7900–00.1022	11.86 ± 0.01	11.27 ± 0.01	10.68 ± 0.01	25.03 ± 0.31	28.5 ± 0.23	13.65 ± 0.64	53.31 ± 1.68

Table 6. Mean FIR colours of the CORNISH-PNe are shown in column 3 and the mean colours in column 2 are from Anderson et al. (2012) PNe samples. The error is the standard deviation.

Colour	Anderson et al. (2012)	CORNISH-PNe
Log_{10}[12/8]	0.57 ± 0.29	0.45 ± 0.30
Log_{10}[70/22]	0.39 ± 0.51	0.34 ± 0.46
Log_{10}[160/12]	0.80 ± 0.49	0.77 ± 0.67
Log_{10}[160/24]	0.22 ± 0.55	0.02 ± 0.62

The heating mechanism of dust grains in PNe is believed to be by direct stellar emission from the central stars, which can extend beyond the ionized region, and by Ly α radiation within the ionized region (Pottasch et al. 1984; Kwok et al. 1986; Pottasch 1986; Hoare 1990; Van de Steene 2017). Following this, compact and younger PNe, where dust grain heating is mainly by direct stellar emission from their relatively cooler central stars, could show warmer dust temperatures in the range of ∼110 K < T_d < 200 K (Pottasch et al. 1984; Kwok et al. 1986; Pottasch 1986; Hoare 1990; van Hoof, Oudmaijer & Waters 1997), and more evolved PNe, where the major source of heating is from Ly α radiation, would have relatively cooler dust temperatures in the range of ∼20 K $\lesssim T_d \lesssim$ 120 K (Phillips & Márquez-Lugo 2011; Van de Steene et al. 2015).

The term 'evolved' as used here is relative and according to the analysis of Phillips & Márquez-Lugo (2011), PNe with physical diameters $\lesssim$0.08 pc show dust temperatures as high as 180 K, whereas PNe with larger physical diameters (more evolved) show a range of dust temperatures (∼60 K < T_d < 120 K).

How bright PNe are in the FIR will be determined by the density and mean temperature of the dust in their circumstellar envelopes. Young PNe from massive stars will be brighter in the FIR. This is because of their association with cooler dust (outside the ionized region), ejected during the AGB phase (Kwok 1982; Cox et al. 2011). This is also the case for bipolar PNe whose progenitors are believed to have experienced strong mass-loss during the AGB phase. They are also believed to have a torus that remains neutral for a longer time after ionization (Guzman-Ramirez et al. 2014). However, H II regions are brighter in the FIR and at longer wavelengths because of the larger amount of dust they possess and lower mean dust temperatures, which can be as low as ∼25 K (Anderson et al. 2012).

The use of the Hi-Gal survey together with the MIPSGAL 24 μm, and *WISE* 12 μm and 22 μm should help us identify H II regions present in the CORNISH-PNe, if there are any. The CORNISH-

Downloaded from https://academic.oup.com/mnras/article-abstract/480/2/2423/5056229 by University of Leeds user on 14 November 2018

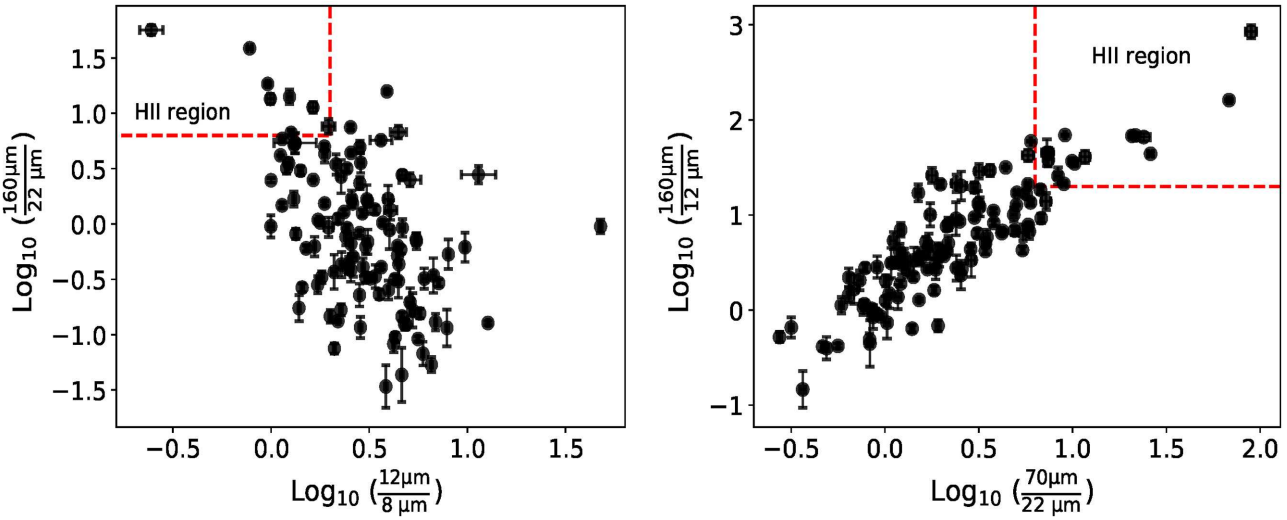

Figure 13. FIR colour–colour plots. Left: $\log_{10}(F_{160}/F_{24})$ versus $\log_{10}(F_{12}/F_8)$. Right: $\log_{10}(F_{160}/F_{12})$ versus $\log_{10}[F_{70}/F_{22}]$. On both plots, we show the cut-off colours (red dotted lines) from Anderson et al. (2012) for H II regions (see Table 6) on the CORNISH-PNe (A colour version of this figure is available in the online journal).

PNe were cross-matched with the Hi-Gal point source catalogue (individual bands) using a generous radius of 20 arcsec and their images were checked to eliminate mis-matches and identifications due to background emission. The CORNISH-PNe were also cross-matched with the *WISE* 12 and 22 μm,[6] and MIPSGAL 24 μm point source catalogue (Gutermuth & Heyer 2015) using the same generous radius of 20 arcsec.

In Table 6, we show the mean colours of CORNISH-PNe compared to the mean colours of PNe sample analysed by Anderson et al. (2012). The mean colours of the CORNISH-PNe show a good agreement with the Anderson et al. (2012) sample within 1σ.

Due to the different mean dust temperatures of the PNe and H II regions, they should occupy distinctly different positions on the FIR colour–colour plots. Based on the analysis of Anderson et al. (2012) on discriminating between H II regions and PNe (see Table 3 in Anderson et al. 2012), we chose the $\log_{10}[F_{160}/F_{24}]$ versus $\log_{10}[F_{12}/F_8]$ and $\log_{10}[F_{160}/F_{12}]$ versus $\log_{10}[F_{70}/F_{22}]$ colour–colour planes. The distributions of the CORNISH-PNe on these colour–colour planes are shown in Fig. 13. A few of the CORNISH-PNe FIR colours extends into the H II region area. This is likely due to sample selection bias as the Anderson et al. (2012) sample is made up of optically detected PNe. Hence, the CORNISH-PNe within the H II region area could be compact PNe with cooler dust outside their ionized regions. At a 3σ significance level, three of the CORNISH-PNe (see Section 4.2) are within the H II regions area on both colour–colour planes.

3.4 Extinction

Extinctions were estimated using the H α line emission, where available, and NIR magnitudes. The different methods used are discussed below.

3.4.1 Hα/5 GHz *ratio*

Both the H α and 5 GHz emissions are assumed to come from the same effective volume of ionized gas, but unlike the hydrogen line emission, the free–free emission is not affected by interstellar extinction. Following this, the extinction was estimated by comparing the radio-continuum emission at 5 GHz to the H α line flux. In estimating the H α line fluxes (Column 5 in Table 3), the continuum contribution was accounted for based on the Sloan filter profile,[7] while ignoring the [N II] contribution. Equation (5) (see Ruffle et al. 2004) was used to estimate the extinction in magnitudes (c_r), which was converted to visual extinction (A_V) using $A_V = 1.2c_r$ (calculated from the Cardelli et al. 1989 extinction curve with $R = 3.1$). The distribution of A_V from this method (for 22 PNe) is shown in Fig. 14 (top panel):

$$c_r\ (\mathrm{mag}) = -2.5\log_{10}\left[\frac{F(\mathrm{H}\alpha)(\mathrm{erg\,cm^{-2}\,s^{-1}})}{9.20\ \times\ 10^{-13}F_{5\,\mathrm{GHz}}(\mathrm{mJy})}\right]. \quad (5)$$

3.4.2 *K/5GHz and H*/5 GHz *ratio*

Extinction can also be determined from the ratio of the NIR to the radio integrated flux density. For this method, the intrinsic flux ratio determined by Willner, Becklin & Visvanathan (1972) ($F_K/F_{5\,\mathrm{GHz}} = 0.3$ and $F_H/F_{5\,\mathrm{GHz}} = 0.26$) was used to determine A_K and A_H in equation (6). The relationship between the NIR extinction (A_K and A_H) and A_V was further derived using the relationships: $A_J/A_V = 0.283$, $A_H/A_V = 0.184$, and $A_K/A_V = 0.113$ (calculated from the Cardelli et al. 1989 extinction curve for $R = 3.1$). This method assumes that emission is due to ionized gas (free–free emission, free-bound, and hydrogen line emissions). In instances where hot dust dominates the emission, which is the case for some very young/dense and compact PNe, A_V will be underestimated using this method. This will result in negative A_V magnitudes for some PNe. Approximately, 38 per cent of the CORNISH-PNe with reliable K-band magnitudes have negative A_V (as low as ~ -33 mag)

[6] http://irsa.ipac.caltech.edu/cgi-bin/Gator/nph-scan?submit=Selectprojshort=WISE

[7] http://svo2.cab.inta-csic.es/svo/theory/main/

Downloaded from https://academic.oup.com/mnras/article-abstract/480/2/2423/5056229 by University of Leeds user on 14 November 2018

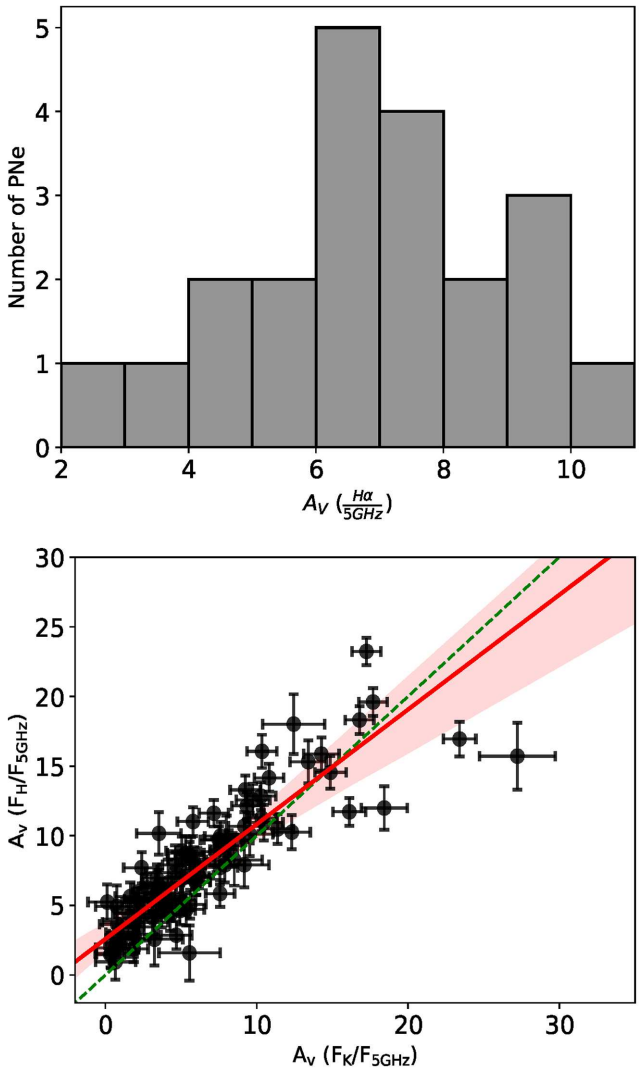

Figure 14. Upper panel: A_V from H $\alpha/F_{5\,\mathrm{GHz}}$ method for the 22 CORNISH-PNe with IPHAS counterparts. Lower panel: A_V from the $F_H/F_{5\,\mathrm{GHz}}$ method against A_V from the $F_K/F_{5\,\mathrm{GHz}}$ method. The regression line is shown in red with a 95 per cent confidence band. Less weight is placed on larger errors. The green line is the one-to-one fit (A colour version of this figure is available in the online journal).

and ∼23 per cent with reliable H-band magnitudes have negative A_V (as low as ∼−18 mag). These sources are not shown on the plot (Fig. 14), but are given in Table 8. This could be the effect of hot dust emission, resulting in larger H- and K-band flux densities, compared to the level of ionized gas. For such CORNISH-PNe, where the effect is more on the K band, $H/5$ GHz will give a better estimation. A comparison between $K/5$ GHz and $H/5$ GHz is shown in Fig. 14 (bottom panel). The difference between the regression line and equality line is <5 mag in A_V.

$$A_K = -1.086 \ln \frac{F_K}{0.3 F_{5\,\mathrm{GHz}}}; \quad A_H = -1.086 \ln \frac{F_H}{0.26 F_{5\,\mathrm{GHz}}}. \qquad (6)$$

3.4.3 E(H − K) and E(J − H)

Extinction determined from the colour excess method normalizes observed colours to intrinsic or expected colours. Using equation (6) (see Section 3.4.2) and the flux ratio determined by Willner et al. (1972) and in Paper III ($F_J/F_{5\,\mathrm{GHz}} = 0.43$), we determined intrinsic colours of $(H-K)_0 \sim 0.68$ and $(J-H)_0 \sim -0.1$. These colours agree with the modelled intrinsic colours of NGC 6270 (0.62, 0.0) determined by Weidmann et al. (2013) and the average intrinsic colours of $(H-K)_0 \sim 0.65$ and $(J-H)_0 \sim -0.1$ from the Galactic PNe sample analysed by Ramos-Larios & Phillips (2005).

The CORNISH-PNe NIR colours were normalized to the derived intrinsic colours of $(H-K)_0 \sim 0.68$ and $(J-H)_0 \sim -0.1$ and A_V was determined using the relationships in Section 3.4.2. In Fig. 15, we present comparison between A_v obtained using $E(J-H)$ and $E(H-K)$ colour excesses. The effect of hot dust is also seen, which is reflected in the difference between the regression line (red) and the equality line (green).

From the analysis presented in Section 3.3, with the likelihood of the CORNISH-PNe being compact and young, we expect some CORNISH-PNe to be dominated by hot dust. In addition to hot dust, the large excesses in the $H-K$ and $F_K/F_{5\,\mathrm{GHz}}$ could also result from H_2 emission within the K band. Hence, larger NIR excesses compared to the expected level for thermal ionized gas. For such sources, their intrinsic colours could be higher than 0.68 $(H-K)$ and −0.1 $(J-H)$. According to Pena & Torres-Peimbert (1987) the intrinsic $H-K$ colour for high density and younger PNe could be as high as 0.8. This is also reflected in the range of intrinsic modeled colours for NGC 7027 (0.21, 0.41) and NGC 6720 (0.62, 0.0) by Weidmann et al. (2013), shown in Fig. 10

In Table Table 7, we compare A_V from the different methods for a few sources. We also perform a literature search for the A_V of a few well-known PNe within the CORNISH-PNe sample. The $F_K/F_{5\,\mathrm{GHz}}$ method appears to result in underestimated A_V compared to other methods and the literature values. However, there are a few CORNISH-PNe whose A_V agree within the stated errors for the different methods. No one method can be considered definitive for each CORNISH-PNe. .

The varying extinctions from these methods can be attributed to the effect of different dominant emissions (see Ramos-Larios & Phillips 2005) as observed in Fig. 10, resulting in the different A_V using the different methods. A_V within lower Galactic latitudes could be as high as ∼30 mag (see the extinction map of González-Solares et al. 2008; Gonzalez et al. 2012), which agrees with the maximum estimated A_V for the CORNISH-PNe using the different methods. A_V estimated from the different methods for the CORNISH-PNe are given in Table 8.

3.5 Heliocentric distances

Heliocentric distances to the CORNISH-PNe were estimated using the statistical distance scale described in Frew, Parker & Bojičić (2016). The integrated flux density of each CORNISH-PNe was converted to H α surface brightness (erg cm^{-2} s^{-1}) and equation (8) in Frew et al. (2016) was used to estimate the physical radii and corresponding distances. It should be noted that equation (8) provides a mean distance and we have not treated optically thin or thick PNe separately (See Frew et al. 2016 for review and details of this statistical distance calibration).

The distributions of the CORNISH-PNe distances and physical sizes are presented in Fig. 16. The distance distribution shows a peak at ∼11 kpc and gradually falls off to 32 kpc. The physical diameter distribution shows a generally compact sample with a peak at 0.17 ± 0.06 pc. The mean physical diameter and heliocentric distance are 0.14 pc and 14 ± 6 kpc, respectively.

In Fig. 17, we show a scatter plot of the distances against the physical diametres and it can be seen that the CORNISH-PNe with

Downloaded from https://academic.oup.com/mnras/article-abstract/480/2/2423/5056229 by University of Leeds user on 14 November 2018

Table 7. Comparison of the A_V from the different methods for some extended sources. Where available, we use literature $H\,\alpha$ or $H\,\beta$ fluxes to calculate A_V. Where c (extinction constant) is given in the literature, we converted to A_V using $c/E(B-V) = 1.46$. Asterisk (∗) indicates that the $H\,\alpha$ is from a larger area compared to the radio emission.

Name	Known Name	A_V *Hα/radio*	A_V $E(H-K)$	A_V $E(J-H)$	A_V *K/radio*	A_V *H/radio*	A_V Literature
G010.0989+00.7393	NGC 6537	–	3.56 ± 0.56	4.97 ± 0.34	1.96 ± 0.95	2.62 ± 0.95	3.71[1], 3.78[2], 4.3[3]
G035.4719–00.4365	–	8.68 ± 0.29	5.63 ± 0.20	8.68 ± 0.14	4.32 ± 0.95	4.87 ± 0.95	–
G050.5556+00.0448	–	11.60 ± 0.41	11.26 ± 0.25	11.04 ± 0.20	7.25 ± 0.96	8.85 ± 0.97	–
G051.8341+00.2838	–	9.53 ± 0.31	8.76 ± 0.32	8.33 ± 0.15	5.92 ± 0.91	7.07 ± 0.90	–
G055.5070–00.5579	M 1-71	3.45 ± 0.11	4.04 ± 0.58	2.95 ± 0.14	0.96 ± 0.99	2.18 ± 0.93	4.46[4]
G059.8236–00.5361	–	6.81 ± 0.22	7.26 ± 0.32	6.01 ± 0.27	3.94 ± 0.92	5.26 ± 0.91	–
G062.4936–00.2699	M 2-48	2.30 ± 0.08∗	6.34 ± 0.35	6.55 ± 0.21	5.61 ± 1.03	5.08 ± 1.03	4.67[4]
G062.7551–00.7262	–	4.95 ± 0.18	5.96 ± 0.29	7.70 ± 0.21	4.95 ± 1.03	5.38 ± 1.04	

[1]Matsuura et al. (2005), [2]Pottasch, Beintema & Feibelman (2000), [3]Kaler (1983), [4]Tylenda et al. (1992).

Table 8. Extinction table showing A_V from the different methods in Section 3.4 for all the CORNISH-PNe. Sources whose $H\,\alpha$ emission area is larger than radio, we have indicated using *. Full table available online as Table A3.

CORNISH name	$\mathrm{H}\,\alpha/F_{5\,\mathrm{GHz}}$	$E(H-K)$	$E(J-H)$	$F_{\mathrm{H}}/F_{5\,\mathrm{GHz}}$	$F_K/F_{5\,\mathrm{GHz}}$
G009.9702–00.5292	–	13.29 ± 0.47	17.74 ± 0.4	5.24 ± 1.26	0.12 ± 1.26
G010.0989+00.7393	–	3.56 ± 0.57	4.97 ± 0.34	2.62 ± 0.96	1.97 ± 0.96
G010.4168+00.9356	–	2.71 ± 0.58	7.77 ± 0.35	− 0.4 ± 1.09	− 2.39 ± 1.09
G010.5960–00.8733	–	16.07 ± 0.62	22.31 ± 0.37	7.71 ± 1.12	2.39 ± 1.18
G011.3266–00.3718	–	10.6 ± 0.26	24.32 ± 0.38	3.49 ± 1.75	− 1.03 ± 1.75
G011.4290–01.0091	–	1.99 ± 0.33	− 0.43 ± 0.24	− 11.49 ± 1.39	− 19.89 ± 1.37
G011.4581+01.0736	–	3.7 ± 0.25	15.54 ± 0.2	− 0.99 ± 1.55	− 3.96 ± 1.55
G011.7210–00.4916	–	–	–	–	–
G011.7434–00.6502	–	5.29 ± 0.2	2.78 ± 0.14	− 1.15 ± 0.96	− 5.21 ± 0.96
G011.7900–00.1022	–	− 1.24 ± 0.2	6.98 ± 0.14	− 6.42 ± 1.67	− 9.66 ± 1.67

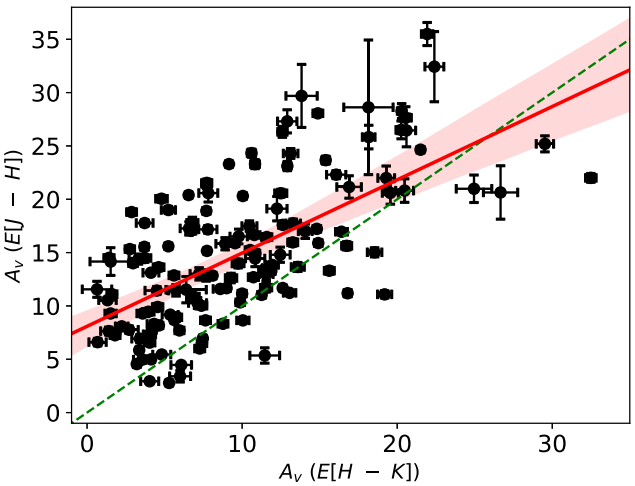

Figure 15. A_V from the colour excess methods, showing A_V from $E(J-H)$ against $E(H-K)$. The regression line is shown in red with a 95 per cent confidence band. The green line is the one-to-one fit. Less weight is placed on larger errors (A colour version of this figure is available in the online journal).

smaller angular sizes, having corresponding small physical sizes (<0.2 pc) are spread over a range of distances and are also the CORNISH-PNe seen at larger distances. The distances to these angularly small CORNISH-PNe are possibly overestimated, given that we have not taken into account the PNe that are optically thick. Estimated distances and physical diametres are presented in Table 9.

Table 9. Distances and physical diameters estimated for the CORNISH-PNe. For the angular sizes whose deconvolved sizes could not be determined, we have stated the upper (<) and lower limits (>) for the distances and physical diameters, respectively. Full table available online as Table A4.

CORNISH name	$\mathrm{Log}_{10}R$ (pc)	Distance (kpc)
G009.9702–00.5292	−0.73 ± 0.06	15.52 ± 2.29
G010.0989+00.7393	−0.93 ± 0.04	3.65 ± 0.33
G010.4168+00.9356	−0.98 ± 0.05	23.00 ± 2.65
G010.5960–00.8733	−0.80 ± 0.05	10.71 ± 1.20
G011.3266–00.3718	−0.63 ± 0.08	12.12 ± 2.15
G011.4290–01.0091	−0.70 ± 0.07	13.45 ± 2.29
G011.4581+01.0736	−0.73 ± 0.08	20.20 ± 3.79
G011.7210–00.4916	−0.68 ± 0.10	20.50 ± 4.90
G011.7434–00.6502	−0.79 ± 0.04	4.93 ± 0.47
G011.7900–00.1022	−0.59 ± 0.07	6.57 ± 1.10

4 DISCUSSION

4.1 Reliability and completeness

Understanding the evolution and formation of PNe requires the reasonable sampling of different stages of their evolution, including the very young PNe, where the shaping mechanism may still be active. Surveys at optical wavelengths have greatly improved the number of known PNe, but these samples are biased by extinction. From the number of currently catalogued PNe (3540; Parker et al. 2017) compared to the predicted number from population synthesis (46 000± 13 000; Moe & De Marco 2006) in our Galaxy, it is clear that many Galactic PNe are yet to be detected, especially towards the Galactic mid-plane where extinction is severe. To improve on

Downloaded from https://academic.oup.com/mnras/article-abstract/480/2/2423/5056229 by University of Leeds user on 14 November 2018

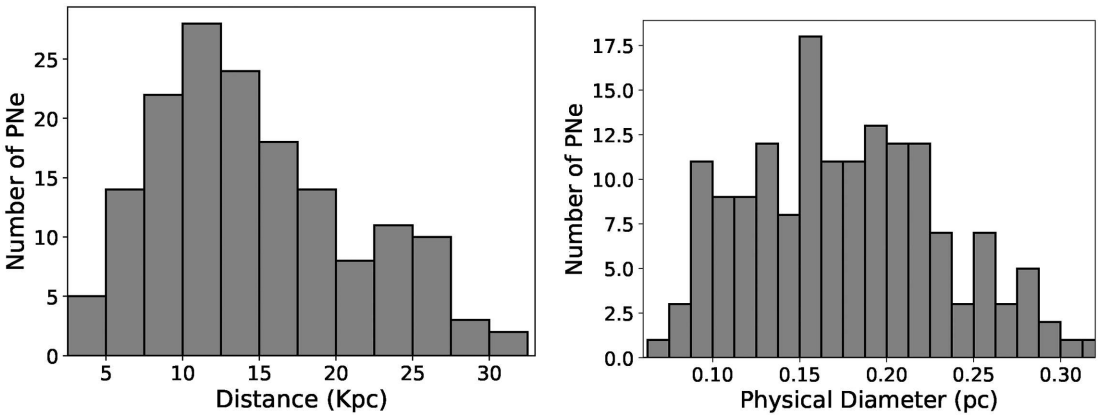

Figure 16. Distribution of the distances in kpc (left) and physical diameters in pc (right).

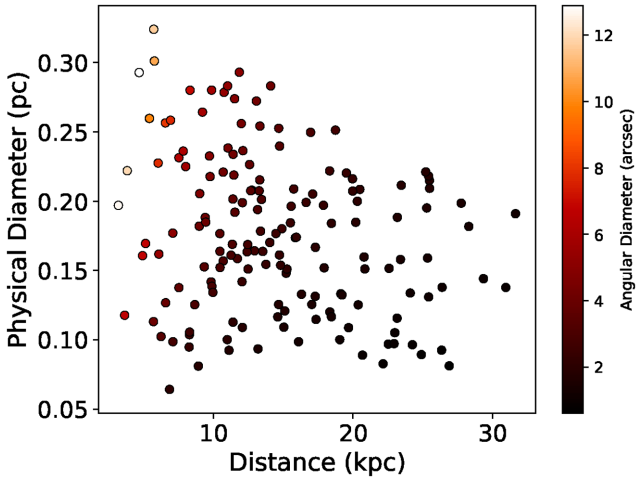

Figure 17. Distances against physical sizes for the CORNISH-PNe. The colour and size of each bubble represents the corresponding angular size (A colour version of this figure is available in the online journal).

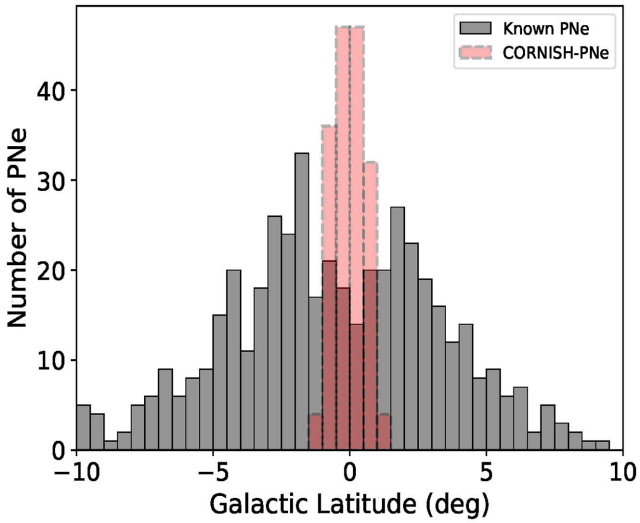

Figure 18. Galactic latitude distribution of the CORNISH-PNe (red) and known PNe (grey). Known PNe samples are from HASH data base (Parker et al. 2017) and includes PNe samples from the Strasbourg-ESO Catalogue of Galactic PNe (Acker et al. 1992), Catalogue of Galactic PNe by Kohoutek 2001, Macquarie/AAO/Strasbourg Halpha Planetary Nebula Catalogues (MASH I, Parker et al. 2006 and MASH II, Miszalski et al. 2008) and IPHAS catalogue (Sabin et al. 2014) (A colour version of this figure is available in the online journal).

the number of known PNe, it is important that PNe are searched for at longer wavelengths. The CORNISH observations at 6 cm provides us with a sample of PNe that is not affected by extinction.

The reliability of this sample has been demonstrated by the multiwavelength visual identification performed by the CORNISH team and the multiwavelength properties presented in this work. To demonstrate the completeness and depth of the CORNISH survey, we have compared the CORNISH-PNe with samples of known PNe in the HASH data base (Parker et al. 2017). This catalogue includes PNe samples from the Strasbourg-ESO catalogue of Galactic PNe (Acker et al. 1992), catalogue of Galactic PNe by Kohoutek (2001), Macquarie/AAO/Strasbourg H α planetary nebula catalogues (MASH I, Parker et al. 2006 and MASH II, Miszalski et al. 2008), and IPHAS catalogue (Sabin et al. 2014).

In Fig. 18, we show the distribution of the CORNISH-PNe and known PNe. Compared to the CORNISH-PNe, the detection of known PNe (optical detections) drops towards $b = 0^{\circ}$, whereas the CORNISH-PNe clearly peak about $b = 0^{\circ}$. This is likely due to the extinction bias associated with optically detected PNe and increased reddening in this region (see the extinction map of Gonzalez et al. 2012).

Furthermore, if we assume a distance of 20 kpc and that PNe can become optically thin at physical diameters >0.12pc (Zijlstra 1990), we would expect corresponding 5 GHz peak fluxes (equation 1 in Stanghellini, Shaw & Villaver 2008) as shown in Fig. 19. At this distance of 20 kpc (see 4σ detection limit as red line in Fig. 19), we could have detected all sources with angular sizes <2.5 arcsec and above the CORNISH survey detection limit. This is reflected in Fig. 17, where CORNISH-PNe with small angular sizes are detected at larger distances. At closer distances (10 and 15 kpc are shown in Fig. 19), we would detect sources with larger angular sizes if their peak fluxes are above the detection limit.

4.2 Combined colour–colour plots

The difficulty in spectroscopic confirmation of PNe due to extinction has informed the need for other methods of confirmation. The works of Cohen et al. (2011) and Parker et al. (2012), using the MASH PNe have shown that the use of multiwavelength analysis can be robust in identifying PNe not detected at optical wavelengths, especially

Downloaded from https://academic.oup.com/mnras/article-abstract/480/2/2423/5056229 by University of Leeds user on 14 November 2018

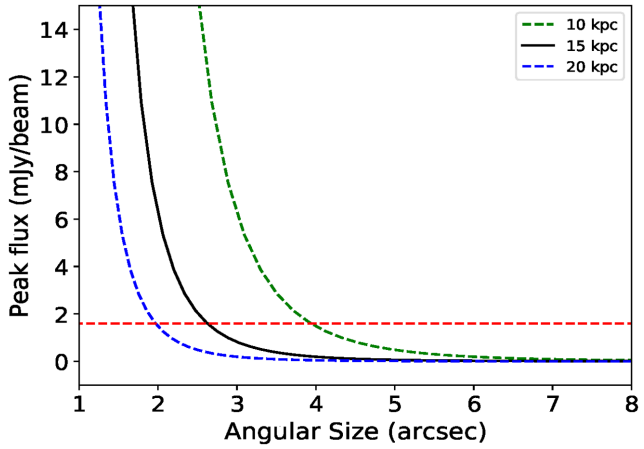

Figure 19. Flux densities at 5 GHz against angular sizes (arcsec) for PNe with physical radii >0.12pc (optically thin PNe), at a distance of 10, 15, and 20 kpc. The red horizontal line represents the 4σ detection limit of the CORNISH survey.

when they have reliable MIR and radio emission measurements. We expect that the multiwavelength colour–colour plots, together with the MIR/radio ratio used in this analysis, should flag different contaminants.

In the NIR colour–colour plot (see Fig. 10), the CORNISH-PNe show a wide range of colours, which agrees with the wide range of unreddened PNe colours analysed by Ramos-Larios & Phillips (2005). In the MIR (Fig. 12), the CORNISH-PNe seem well separated from the symbiotic stars, except for the D-types (dusty). In the FIR, a few CORNISH-PNe extend into the HII regions area on both colour–colour plots. The three outliers in the FIR colour–colour plots (Fig. 13) are G019.2356+00.4951, G052.1498–00.3758, and G058.1591–00.5499. G019.2356+00.4951 also has a negative spectral index and is discussed in Section 4.3.

Despite its FIR colours ($\log_{10}[160/24] \sim 1.54$; $\log_{10}[70/22] \sim 1.83$), G052.1498–00.3758 has no millimetre emission and so it is not likely an HII region (see Fig. 20), with a spectral index of -0.36 ± 0.09. G058.1591–00.5499 has no millimetre data but, its multiwavelength images (Fig. 21), NIR, and MIR colours are consistent with PNe colours.

4.3 Sources with negative spectral indices

The dominant radio continuum emission in an ionized nebulae is expected to be thermal, although some conditions and processes such as jets and magnetic fields in very young PNe could provide an environment for non-thermal emission. Variability at radio wavelengths could also result in non-thermal emission (see Cerrigone et al. 2011, 2017).

The presence of high velocity collimated jets, believed to be the primary shaping mechanism in PNe, could induce shock fronts and accelerate electrons to a relativistic velocity in a magnetic field, which could result in non-thermal emission. Observational evidence of this is seen in a post-AGB source (IRAS 15445-5449) with strong magnetic fields, where ionization has not started, but jets are present (Pérez-Sánchez et al. 2013). Here, we discuss the two CORNISH-PNe with significant negative spectral indices (see Fig. 8; middle panel).

4.3.1 G019.2356+00.4951

G019.2356+00.4951 is classified in the SIMBAD data base G158 as a radio source (MAGPIS and NVSS surveys). It is associated with an X-ray emission (XGPS-I J182416-115554; 3XMM J182416.7-115558,[8] Rosen et al. 2016) in the *XMM–Newton* Galactic Plane Survey (within 4 arcsec search radius), having a hardness ratio of 0.72 (Hands et al. 2004). Although it is isolated in the far-infrared image (Fig. 22), it has FIR colours ($\log_{10}[160/24] \sim 1.28$; $\log_{10}[70/22] \sim 1.32$) expected of H II regions but with no millimetre emission. It can be seen in Fig. 22 that this is an extended source in the MIR and NIR but the CORNISH survey has detected only the bright core.

One of the mechanisms through which X-ray emission is produced in PNe is thought to be related to their shaping mechanisms (wind-wind interaction), resulting in hot bubble formation. Such X-ray emissions is observed within the bright innermost shell. The presence of collimated jets and outflows can also result in shocks that emit X-rays. X-ray emission from such processes are thought to be characteristics of young and compact PNe (Chu et al. 2000; Kastner 2007; Kastner et al. 2008; Freeman et al. 2014).

According to Freeman et al. (2014), PNe that emit X-rays from such interactions are mainly elliptical. G019.2356+00.4951 has an elliptical morphology in the radio, NIR and MIR (see multiwavelength images in Fig. 22) with a spectral index of -0.66 ± 0.09 that is compatible with synchrotron emission. We estimated a distance of $\sim 9 \pm 1$ kpc and a diametre of $\sim 0.18 \pm 0.02$ pc. We classified this source as a PN and it is likely a young PN, based on the X-ray emission and elliptical morphology. The SED of this source is shown in Fig. 24 (top panel).

4.3.2 G030.2335–00.1385

This is an unresolved source in the CORNISH survey with T_b that approximates 10^4 K and a spectral index of -0.55 ± 0.08. This negative spectral index is not due to variability as it has a MAGPIS 6 cm integrated flux density of 348.57 mJy (360.00 ± 32.91 mJy in the CORNISH). It is not detected in the IPHAS survey. Massive stars are known to evolve fast enough to ionize their circumstellar envelope, while the envelopes are still dense (Kwok 1993; Phillips 2003). This source was previously classified as an H II region in Leto et al. (2009), but it is isolated in the FIR image, with no millimetre dust emission. It is classified as a PN by Cooper et al. (2013) from its NIR spectrum and its multiwavelength images (Fig. 23) supports this classification. It is also associated with water (H_2O) maser emission, having a spread of $\sim$70 Km s^{-1}, which supports a young nature. We estimate a distance of $\sim 7.0 \pm 0.6$ kpc and a diameter of $\sim$0.06 pc. The SED of this source is shown in Fig. 24 (bottom panel).

Collimated jets have been observed to be traced by H_2O maser components in post-AGB sources. The velocity spread of these masers can be as wide as ~ 500 km s^{-1}, as observed towards IRAS 18113-2503 (Gómez et al. 2011). The presence of H_2O masers in PNe is indicative of a young nature. A few PNe with negative spectral indices have also been reported in Bojičić et al. (2011). The first observational evidence of non-thermal emission in a PN with H_2O maser emission was seen in IRAS 15103-5754, with a spectral index of $\simeq -0.54 \pm 0.08$ (Suarez et al. 2015) that is compatible with synchrotron emission. IRAS 15103-5754 is presently considered to

[8] http://xmm-catalog.irap.omp.eu/source/200519401010016

Downloaded from https://academic.oup.com/mnras/article-abstract/480/2/2423/5056229 by University of Leeds user on 14 November 2018

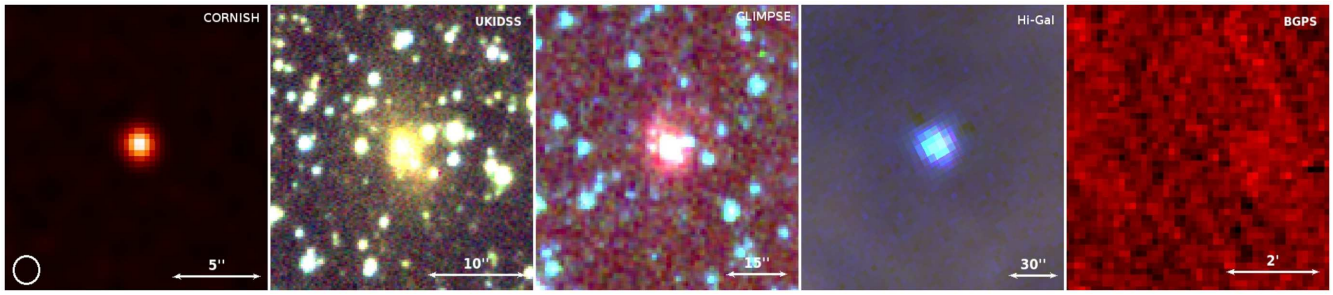

Figure 20. Multiwavelength images of G052.1498–00.3758. We show the CORNISH 5 GHz radio image (left), followed by NIR three-colour images: *J* band is blue, *H* is green, and *K* is red; MIR three-colour image: 3.6 μm is blue, 4.5 μm is green, and 8.0 μm is red; and FIR three-colour image (right): 70 μm is blue, 160 μm is green, and 250 μm is red and the BGPS 1.1 mm. G052.1498–00.3758 has FIR colours that are similar to HII regions (A colour version of this figure is available in the online journal).

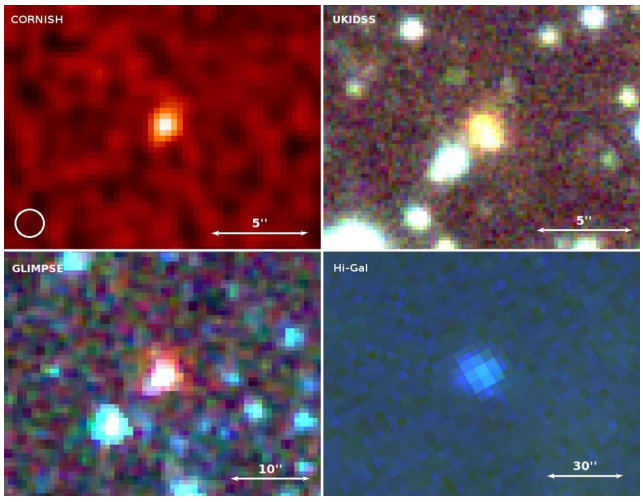

Figure 21. Multiwavelength images of G058.1591–00.5499. We show the CORNISH 5 GHz radio image (top left), NIR three-colour images (top right): *J* band is blue, *H* is green, and *K* is red; MIR three-colour image (bottom left): 3.6 μm is blue, 4.5 μm is green, and 8.0 μm is red; and FIR three-colour image (bottom right): 70 μm is blue, 160 μm is green, and 250 μm is red. G058.1591–00.5499 has FIR colours that are similar to HII regions (A colour version of this figure is available in the online journal).

be the youngest PN. G030.2335–00.1385 shares similar characteristics with IRAS 15103-5754 and will be a good source to investigate further.

Sources with such negative spectral indices could be confused with supernovae remnants (SNRs), having typical spectral indices ≤ -0.5 and X-ray emission (Anderson et al. 2017; Bozzetto et al. 2017). However, there is no known detection of the 22 GHz H_2O maser emission towards SNRs (Claussen et al. 1999; Woodall & Gray 2007), which rules out the possibility of G030.2335–00.1385 being an SNR.

Young SNRs peak at shorter wavelengths (20–50 μm) (Williams & Temim 2016) than PNe, while older or more evolved SNRs have FIR and sub-millimetre emission (Lakićević et al. 2015; Matsuura et al. 2015). The colours (NIR to FIR) of G019.2356+00.4951 are rather consistent with PNe (see Reach et al. 2006; Pinheiro Gonçalves et al. 2011). If it were a core-collapse SNR or PWNe (pulsar wind nebula), we would expect some sub-millimetre emission or a flatter radio spectrum (see Bietenholz et al. 1997; Gaensler & Slane 2006) compared to its steep spectral index of -0.66 ± 0.09.

5 CORNISH-PNE CATALOGUE

PNe in the HASH data base (Parker et al. 2017) have mean and median angular sizes of 44 and 15 arcsec, respectively. The median angular size of PNe for both the MASH and IPHAS catalogues is ∼22 arcsec (Parker et al. 2006; Sabin et al. 2014). It can be seen that known PNe, which are optically selected, are biased towards extended and/or more evolved PNe that may be absent or resolved out in the CORNISH survey. For the CORNISH-PNe, the mean and median angular size are ∼3 and ∼2.5 arcsec, indicating a compact PNe sample that is probably more complete within the $|b| < 1^\circ$ region.

The classification of the CORNISH-PNe was done based on the radio properties, MIR/radio ratio, optical colours, infrared colours, extinction, physical sizes, and distances. In the absence of IPHAS images, we have used the Hα images from the SuperCosmos Hα survey (SHS; Parker et al. 2005),[9] where available, to aid classification. In cases where we are unable to draw conclusions from this analysis, we have indicated possible PNe with a question mark '?', and where truly in doubt, we have tagged 'unknown' or other source type. Sources that meet all requirements for PNe in all considered multiwavelength analysis and images are classified as PNe. We indicate if PNe are newly confirmed, newly classified or newly discovered under the status column. The newly confirmed PNe are sources previously classified as possible PNe or PNe in the SIMBAD data base G158, newly classified are sources previously identified as radio sources or YSO (young stellar objects) in the SIMBAD data base G158, with no previous classification as PN, while newly discovered are sources with no astronomical record in the SIMBAD data base G158. The final catalogue is presented in Table 11 and the columns are defined as follows: CORNISH name (1), SIMBAD identification (2), Hα detection (3), classification (4), status (5), and comments (6).

A cross-match of the 169 CORNISH-PNe with known PNe (True PNe) from HASH data base (Parker et al. 2017) returns 24 matches (Table 10), excluding the CORNISH candidates and likely PNe. A further 47 suspected PNe, as classified in the SIMBAD data base G158, are confirmed as such from the analysis here (see Table 11 for references). 90 out of the remaining 98 CORNISH-PNe are new PNe (12 newly discovered and 78 are newly classified) and the remaining 8 are classified as possible PNe or other source types.

Independently, Fragkou et al. (2017) have used visual inspection of the multiwavelength images on the HASH data base (Parker et al.

[9] http://www-wfau.roe.ac.uk/sss/

Downloaded from https://academic.oup.com/mnras/article-abstract/480/2/2423/5056229 by University of Leeds user on 14 November 2018

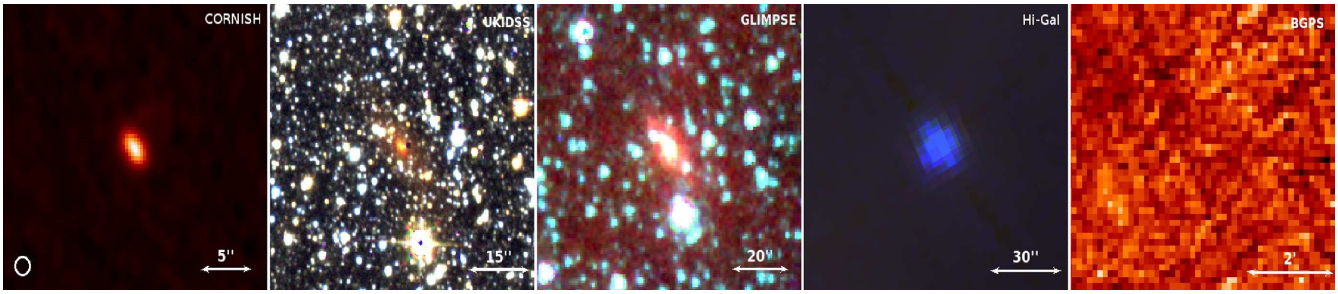

Figure 22. Multiwavelength images of G019.2356+00.4951. We show the CORNISH 5 GHz radio image (left), followed by NIR three-colour images: *J* band is blue, *H* is green, and *K* is red; MIR three-colour image: 3.6 μm is blue, 4.5 μm is green, and 8.0 μm is red; FIR three-colour image (right): 70 μm is blue, 160 μm is green, and 250 μm is red; and the BGPS 1.1 mm. G019.2356+00.4951 has a negative spectral index of -0.66 ± 0.09 that is compatible with synchrotron emission (A colour version of this figure is available in the online journal).

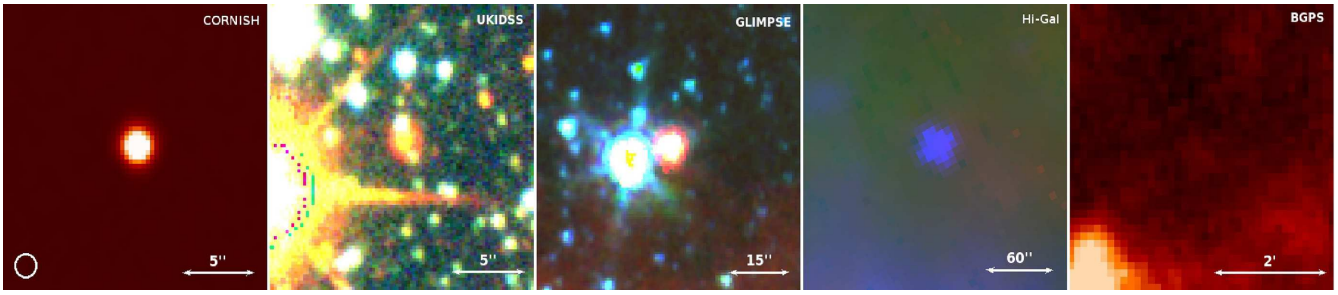

Figure 23. Multiwavelength images of G030.2335–00.1385. We show the CORNISH 5 GHz radio image (left), followed by NIR three-colour images: *J* band is blue, *H* is green, and *K* is red; MIR three-colour image: 3.6 μm is blue, 4.5 μm is green, and 8.0 μm is red; FIR three-colour image (right): 70 μm is blue, 160 μm is green, and 250 μm is red; and the BGPS 1.1 mm. G030.2335–00.1385 has a negative spectral index of -0.55 ± 0.08 (A colour version of this figure is available in the online journal).

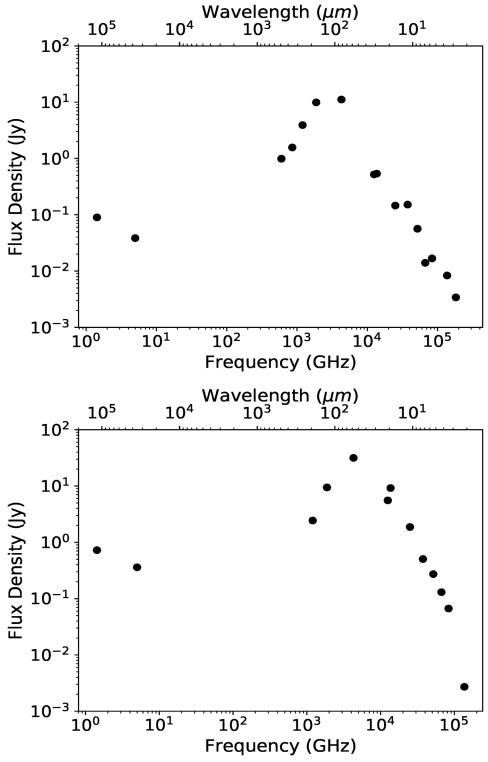

Figure 24. SED (spectral energy distribution) of G019.2356+00.4951 (top) and G030.2335–00.1385 (bottom).

Table 10. 24 Known PNe present in the CORNISH-PNe sample.

CORNISH name	PNG	Other names
G010.0989+00.7393	010.1 + 00.7	NGC 6537
G011.7434–00.6502	011.7 – 00.6	NGC 6567
G011.7900–00.1022	011.7 + 00.0	M 1–43
G012.3315–00.1806	012.3 – 00.1	F2BP 1
G018.0661+00.8535	018.0 + 00.8	IRAS18179−1249
G019.5326+00.7308	019.5 + 00.7	GLIPN1823−1133
G019.9448+00.9126	019.9 + 00.9	M 3–53
G020.4681+00.6793	020.4 + 00.6	PM 1–231
G021.8201–00.4779	021.8 – 00.4	M 3–28
G022.2211+00.9009	022.2 + 00.9	IRAS18257−0908
G026.8327–00.1516	026.8 – 00.1	MPAJ1840−0529
G027.6635–00.8267	027.6 – 00.8	PHRJ1844−0503
G027.7016+00.7048	027.7 + 00.7	M 2–45
G029.2113–00.0689	029.2 + 00.0	TDC1
G032.5485–00.4739	032.5 – 00.4	MPAJ1852−0033
G033.4543–00.6149	033.4 – 00.6	GLMP 844
G050.0405+01.0961	050.0 + 01.0	IRAS19171+1536
G051.5095+00.1686	051.5 + 00.2	KLW 1
G051.8341+00.2838	051.8 + 00.2	IPHASJ192553.5+165331
G055.5070–00.5579	055.5 – 00.5	M 1–71
G056.4016–00.9033	056.4 – 00.9	K 3–42
G059.3987–00.7880	059.4 – 00.7	PM 1–313
G062.4936–00.2699	062.4 – 00.2	M 2–48
G063.8893+00.1229	063.8 + 00.1	K 3–48

Downloaded from https://academic.oup.com/mnras/article-abstract/480/2/2423/5056229 by University of Leeds user on 14 November 2018

Table 11. Final catalogue of the CORNISH-PNe with classifications.

Name	SIMBAD ID	Hα detection	class	Status	Comments
G009.9702–00.5292	pAG[1] (IRAS 18066−2034)	–	PN	Newly classified	
G010.4168+00.9356	pAG[2] (IRAS 18021−1928)	SHS	PN	Newly classified	
G010.5960–00.8733	star (IRAS 18092−2012)	–	PN	Newly classified	
G011.3266–00.371	YSO?[3]	–	PN	Newly classified	
G011.4290–01.0091	–	–	PN	Newly discovered	
G011.4581+01.0736	pAG[1] (IRAS 18038−1830)	–	PN	Newly classified	
G011.7210–00.4916	–	–	PN?	Newly discovered	FIR colours are upper limits
G012.0438–00.5077	–	–	PN?	Newly discovered	FIR colours are upper limits
G012.1157+00.0757	Radio source[4]	SHS	PN	Newly classified	
G012.1528–00.3304	YSO?(J18132367−1833495)[3]	–	PN	Newly classified	
G012.3830+00.7990	PN?[6] (IRAS 18067−1749)	–	PN	Newly confirmed	
G012.6012+00.5592	YSO?[3] (IRAS 18081−1745)	–	PN	Newly classified	
G013.3565–00.7559	YSO?[3]	–	PN	Newly classified	
G013.6313–00.6023	Radio source[4]	–	PN	Newly classified	
G013.9166+00.6500	PN?[7]	–	PN	Newly confirmed	
G014.2365+00.2117	PN?[8]	SHS	PN	Newly confirmed	
G014.4573–00.1847	Radio source[9]	–	PN	Newly classified	
G014.5851+00.4613	PN?[21]	IPHAS	PN	Newly confirmed	
G014.7503–00.2496	Radio source[9]	–	PN	Newly classified	
G014.8960+00.4837	YSO?[3]	SHS	PN	Newly classified	
G015.1999–00.0863	Radio source[9]	–	PN	Newly classified	
G015.5410+00.3359	Radio source[9]	–	PN	Newly classified	
G015.5847+00.4002	Radio source[9]	–	PN	Newly classified	
G015.7993–00.0063	PN[8]	–	PN	Newly confirmed	
G016.0550+00.8280	PN[8]	SHS	PN	Newly confirmed	
G016.4034–00.5740	Radio source[4]	–	PN	Newly classified	
G016.4276+01.0072	–	–	PN	Newly discovered	
G016.4999+00.1152	Radio source[4]	–	PN	Newly classified	NIR colours have stellar contamination
G016.6002–00.2754	Radio source[9]	–	PN	Newly classified	
G017.0152–00.1906	Radio source[9]	–	PN	Newly classified	
G017.3669+00.5224	PN?[10]	–	PN	Newly confirmed	
G017.4147+00.3791	Radio source[4]	–	PN	Newly classified	
G017.4487+00.1146	Radio source[9]	–	PN	Newly classified	
G017.7250–00.2427	Radio source[9]	SHS	PN	Newly classified	
G017.8222+00.9866	–	SHS	PN	Newly discovered	
G017.8645+00.2120	YSO?[3] (IRAS 18198−1318)	–	PN	Newly classified	
G018.1286–00.2189	–	–	PN?	Newly discovered	FIR are upper limits
G018.2402–00.9152	PN[8]	IPHAS	PN	Newly confirmed	
G018.2413–00.5552	YSO?[3]	–	PN	Newly classified	Has no FIR colours
G018.5242+00.1519	YSO?[5]	–	PN	Newly classified	
G018.5776–00.7484	–	–	PN	Newly confirmed	
G019.2356+00.4951	Radio source[4]	–	PN	Newly classified	
G019.4676–00.0154	Radio source[9]	–	PN	Newly classified	
G019.9298–00.6639	IR (IRAS 18270−1153)	–	PN	Newly classified	
G020.5176+00.4778	Radio source[4]	SHS	PN	Newly classified	
G020.6015+00.0206	–	–	PN	Newly discovered	Very resolved in the CORNISH survey compared to the MAGPIS but a clear nebula in the 24 μm. Heavy stellar contamination in the NIR and MIR
G020.9782+00.9253	PN?	SHS	PN	Newly confirmed	
G021.1653+00.4755	PN[8] (IRAS 18252−1016)	SHS	PN	Newly confirmed	
G021.3425–00.8423	PN[8] (IRAS 18303−1043)	–	PN	Newly confirmed	
G021.6657+00.8110	PN[20]	IPHAS	PN	Newly confirmed	
G021.6849–00.7381	Radio source[4]	SHS	PN	Newly confirmed	
G021.9972–00.8838	–	–	PN	Newly discovered	
G022.5477–00.1061	Radio source[9]	–	PN	Newly classified	
G022.6429–00.4422	YSO?[3]	–	PN	Newly classified	
G022.6580+00.2959	Radio source[9]	–	PN	Newly classified	
G023.2321+00.0809	Radio source[9]	–	PN	Newly classified	
G023.4181–00.3940	PN[8] (IRAS 18326−0840)	–	PN	Newly confirmed	

Downloaded from https://academic.oup.com/mnras/article-abstract/480/2/2423/5056229 by University of Leeds user on 14 November 2018

Table 11 – *continued*

Name	SIMBAD ID	Hα detection	class	Status	Comments
G023.5044–00.5245	Star (IRAS 18332−0839)[4]	–	PN	Newly classified	
G023.8214–00.5788	PN[8]	–	PN	Newly confirmed	
G023.8897–00.7379	PN[11] (IRAS 18347−0825)	–	PN	Newly confirmed	
G024.0943–01.0992	–	–	Radio star?	Newly discovered	Upper limits on FIR colours
G024.1659+00.2502	H II region[12]	–	PN	Newly classified	
G024.3852+00.2869	PN[8]	–	PN	Newly confirmed	
G024.7921–01.0043	IR(IRAS 18373−0744)	SHS	PN	Newly classified	
G024.8959+00.4586	YSO?[3]	–	PN	Newly classified	
G025.0485–00.6621	PN[7]	–	PN	Newly confirmed	
G025.5190+00.2165	H II region[12]	–	PN	Newly classified	
G025.5769+00.1389	Radio source[9]	–	PN	Newly classified	
G025.8466+01.1718	PN?[11]	–	PN	Newly confirmed	No MIR data but PN colours in NIR and FIR
G026.0823–00.0347	Radio source[9]	–	PN?	Newly classified	Near dark filaments in the MIR but PN colours in the MIR and FIR
G026.1620+00.5926	–	–	PN	Newly discovered	
G026.2268+00.7685	–	–	PN	Newly discovered	
G026.6529+00.2874	Radio source[9]	–	PN	Newly classified	
G026.7145+00.1319	Radio source[9]	–	PN	Newly classified	
G027.4265–00.2499	YSO?[3]	SHS	PN	Newly classified	
G027.6595–00.3835	PN[8] (IRAS 18404−0455)	SHS	PN	Newly confirmed	
G027.6640–00.2485	–	–	PN?Radio star?	Newly classified	
G029.0538+00.9915	YSO?[3]	SHS	PN	Newly classified	
G029.1652–00.0168	Radio source[9]	–	PN	Newly classified	
G029.5780–00.2686	PN[19]	IPHAS	PN	Newly confirmed	
G029.8742–00.8190	PN[8] (IRAS 18461−0309)	–	PN	Newly confirmed	
G030.0226+00.1570	Radio source[9]	–	PN	Newly classified	
G030.0294–00.3318	Radio source[9]	–	PN	Newly classified	
G030.2335–00.1385	PN?[13] (IRAS 18443−0231)	–	PN	Newly confirmed	
G030.5302+00.1315	Radio source[9]	–	PN?	Newly classified	
G030.6670–00.3319	PN[8] (IRAS 18458−0213)	–	PN	Newly confirmed	
G030.8560+00.3826	Radio source[9]	–	PN	Newly classified	
G031.2131–00.1803	OH & H_2O maser[14]	–	PN	Newly classified	
G031.3724–00.7514	PN? (J18511825−0143487)	–	PN	Newly confirmed	
G032.3076+00.1536	PN[13] (IRAS 18471−0032)	–	PN	Newly confirmed	
G032.6136+00.7971	PN?[8]	IPHAS	PN	Newly confirmed	
G032.8082–00.3159	Radio source[9]	–	PN	Newly classified	
G032.8177–00.1165	–	–	PN	Newly discovered	
G033.1198–00.8949	–	–	PN	Newly discovered	
G033.3526+00.4043	YSO?[3](IRAS 18482+0029)	–	PN	Newly classified	
G033.7952+00.4307	YSO?[3]	–	PN	Newly classified	
G033.9059–00.0436	PN[8]	–	PN	Newly confirmed	
G034.1792–00.1777	Radio source[9]	–	PN	Newly classified	
G034.4200–00.3183	PN[8]	–	PN	Newly confirmed	
G034.8624–00.0630	PN[8]	–	PN	Newly confirmed	
G035.2162+00.4280	Radio source[9]	–	PN	Newly classified	
G035.4719–00.4365	Radio source[9]	IPHAS	PN	Newly classified	
G035.5654–00.4922	PN?[22]	IPHAS	PN	Newly confirmed	
G036.0116–00.2562	Radio source[9]	–	PN	Newly classified	
G036.5393+00.2003	Radio source[9]	–	PN	Newly classified	
G037.9031–00.2754	YSO?[3]	–	PN	Newly classified	
G037.9601+00.4534	PN[8]	–	PN	Newly confirmed	
G038.9237–00.0807	Radio source[9]	–	PN	Newly classified	
G039.1617+00.7826	PN?[7]	–	PN	Newly confirmed	
G039.5911–00.3785	–	–	PN	Newly discovered	
G040.2606–00.2755	YSO[8] (IRAS 19034+0618)	–	PN	Newly classified	
G040.3359–01.0102	–	–	PN	Newly discovered	
G041.1982+00.0348	YSO?[3] (IRAS 19040+0717)	–	PN	Newly classified	
G041.3540+00.5390	Radio source[4]	IPHAS	PN	Newly classified	
G041.7871+00.4884	YSO?[3]	–	PN	Newly classified	
G042.6629–00.8648	PN?[15, 7] (PM 1–288)	–	PN	Newly confirmed	
G043.0281+00.1399	PN[8] (IRAS 19071+0857)	–	PN	Newly confirmed	
G043.2946–00.6455	PN[8]	–	PN	Newly confirmed	

Downloaded from https://academic.oup.com/mnras/article-abstract/480/2/2423/5056229 by University of Leeds user on 14 November 2018

Table 11 – *continued*

Name	SIMBAD ID	H α detection	class	Status	Comments
G043.5793+00.0261	PN[13]	–	PN	Newly confirmed	
G043.6554–00.8279	IR (IRAS 19117+0903)	IPHAS	PN	Newly classified	
G044.6375+00.4827	YSO?[3] (IRAS 19089+1032)	IPHAS	PN	Newly classified	
G045.1801+00.9893	Radio source[16]	–	PN	Newly classified	
G045.2830–00.6278	PN[13] (J19163050+1040563)	–	PN	Newly confirmed	
G046.9747+00.2702	YSO?[3] (IRAS 19141+1230)	–	PN	Newly classified	
G047.6884–00.3024	PN[8, 1]	–	PN	Newly confirmed	
G047.9875+00.2026	star (IRAS 19163+1322)	–	PN	Newly classified	
G048.5619+00.9029	YSO?[3]	IPHAS	PN	Newly classified	
G048.6748–00.5350	YSO?[3]	–	PN	Newly classified	
G048.7319+00.9305	PN[19]	IPHAS	PN	Newly confirmed	
G049.6948+00.8642	PN?[17] (J19193387+1516421)	–	PN	Newly confirmed	
G050.0003+00.5072	YSO? [3]	–	PN	Newly classified	
G050.0457+00.7683	PN?[8]	–	H II region?	Newly classified	
G050.4802+00.7056	PN?[19]	IPHAS	PN	Newly confirmed	
G050.5556+00.0448	PN[8]	IPHAS	PN	Newly confirmed	
G050.8950+00.0572	YSO?[3] (J19245196+1557287)	–	PN	Newly classified	
G051.6061+00.9140	YSO?[3] (IRAS 19209+1653)	–	PN	Newly classified	
G052.1498–00.3758	Radio source[4]	–	PN	Newly classified	
G057.5352+00.2266	Radio source[16]	–	PN	Newly classified	
G058.1591–00.5499	Radio source[16]	–	PN	Newly classified	
G058.6410+00.9196	PN[18]–IRAS 19353+ 2302	IPHAS	PN	Newly confirmed	
G059.8236–00.5361	PN?[13] (IRAS 19434+2320)	IPHAS	PN	Newly confirmed	
G060.8480–00.8954	YSO?[3]	–	PN	Newly classified	
G060.9866–00.5698	Radio source[4]	IPHAS	PN	Newly classified	
G062.7551–00.7262	PN[19]	IPHAS	PN	Newly confirmed	
G063.0455+00.5977	–	–	PN	Newly discovered	

Notes. pAG: post−AGB star, SgrS: Super−giant star, IR source: Infrared source. The questionmark (?) in front of some of the source classification indicates 'possible'. e.g pAG? is a possible post-AGB star

[1](Kohoutek 2001), [2](Ratag & Pottasch 1991), [3](Robitaille et al. 2008), [4](Zoonematkermani et al. 1990), [5](Felli et al. 2002), [6](Hoare et al. 2012), [7](Condon et al. 1999), [8](Urquhart et al. 2009b), [9](Becker et al. 1994), [10](Anderson et al. 2011), [11](Kistiakowsky & Helfand 1995), [12](Anderson et al. 2015), [13](Kanarek et al. 2015), [14](Caswell 2001), [15](Preite-Martinez 1988), [16](Taylor et al. 1996), [17](Phillips & Ramos-Larios 2008), [18](van de Steene & Pottasch 1995), [19](Sabin et al. 2014), [20](van de Steene, Jacoby & Pottasch 1996), [21](Miszalski et al. 2008), [22](Parker et al. 2006).

2017), the MIR/radio ratio, and MIR colours to identify 70 of the sources in CORNISH catalogue as candidate PNe.

Some of the intrinsically red sources based on MIR colours from the GLIMPSE I and II surveys that were classified as candidate YSO by Robitaille et al. (2008) turn out to be PNe (also see Parker et al. 2012). YSO are embedded objects with weak radio emission from ionized stellar winds that is usually less than a few mJy (Hoare et al. 1994; Hoare 2002). The 4.8–15GHz radio integrated flux density of the YSO sample from the Red MSX Source Survey (Lumsden et al. 2013) are mostly upperlimits (97 per cent). We estimated a median MIR/radio ratio in order of 10^3, which is high compared to the MASH PNe (Cohen et al. 2011) and CORNISH-PNe value of 4.7 ± 1.1 and 3.9 ± 0.90, respectively. We expect them to also have FIR colours similar to H II regions as they emit more in the MIR to FIR.

Similarly, 10 out of the 27 high-quality candidate PNe identified by Parker et al. (2012), within the CORNISH survey region, are not in the 7σ catalogue. Parker et al. (2012) classified these as high-quality PNe based on the MIR colours of previously known PNe, MIR environment, and MIR false-colour images. Inspection of the CORNISH images shows that they are not reliable PNe candidates (see Fig. 25). Because these sources are compact in the GLIMPSE survey, we can rule out the possibility that a null detection by the CORNISH survey is due to completely resolved out emission. These could possibly be evolved stellar objects or YSO (Oliveira et al. 2013).

6 CONCLUSION

Following the visual selection of the CORNISH-PNe (169) from the CORNISH survey by the CORNISH team, we have focused on their multiwavelength properties, including their radio properties, optical to FIR colours, extinction, and distances. The sensitivity of the CORNISH survey combined with multiwavelength data, at infrared and millimetre wavelengths, provides an uncontaminated sample of PNe that is free from extinction biases associated with optical surveys. At 6 cm, the CORNISH survey is more complete within the $|b| < 1^\circ$ region and has uncovered 90 new and compact Galactic PNe within 110 deg^2 area. Radio-selected samples from such surveys, unaffected by extinction, will be excellent to compare with models of population synthesis. This would contribute to better understanding of the formation and evolution of Galactic PNe. In future work, we will compare this sample, although small, with model predictions from population synthesis. In summary:

– We have used multiwavelength properties to certify the CORNISH-PNe classification and confirm a clean sample, although one will need an optical or NIR spectra to fully confirm the status of a PN.

– Radio properties show a CORNISH-PNe sample that is compact, with some PNe possessing $T_b > 1000$ K. We were able to estimate spectral indices for 127 of the CORNISH-PNe (75 per cent). 98 per cent of these have spectral indices that are consistent with

Downloaded from https://academic.oup.com/mnras/article-abstract/480/2/2423/5056229 by University of Leeds user on 14 November 2018

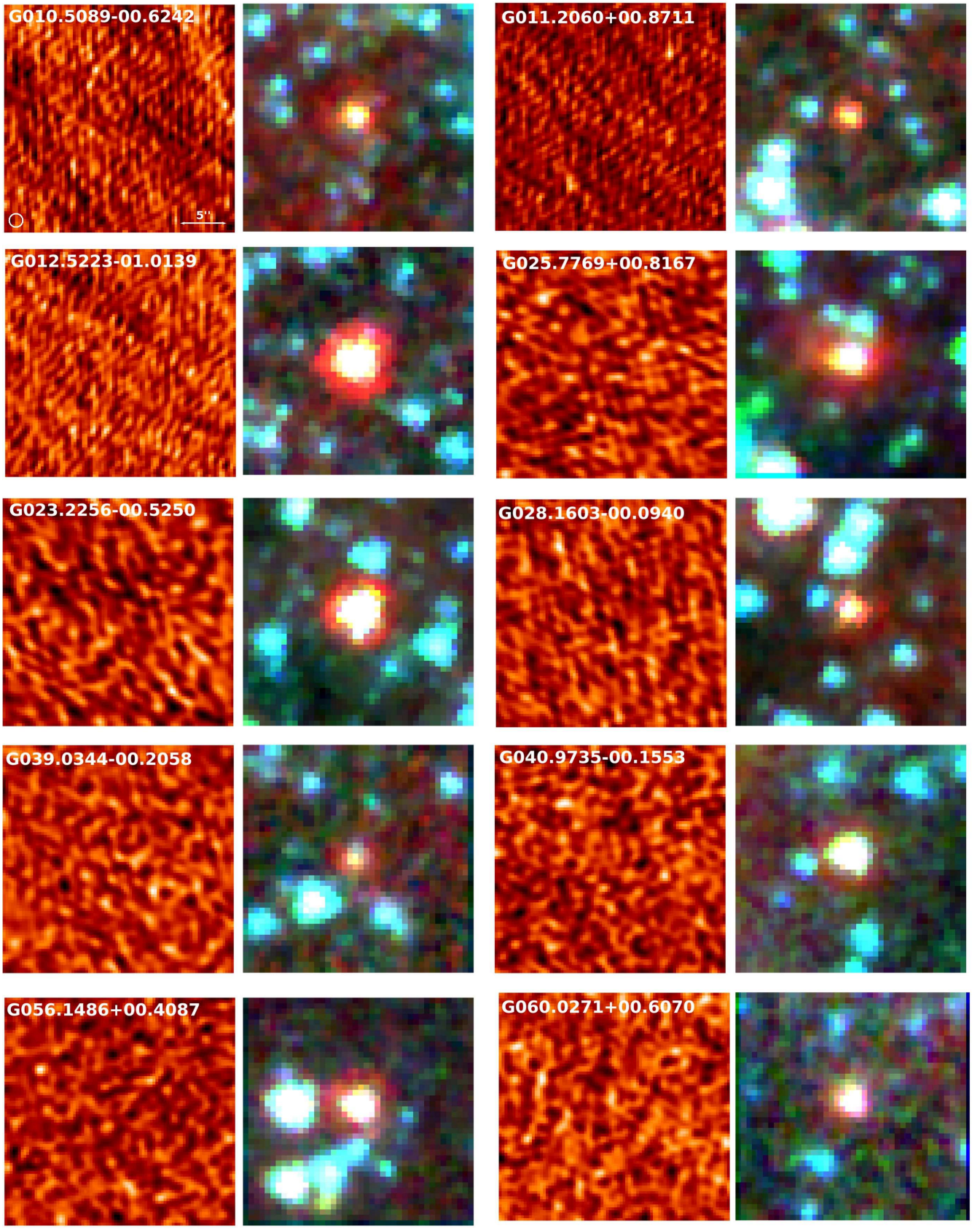

Figure 25. CORNISH 6 cm and three-colour (3.6 μm is blue, 5.8 μm is green, and 8.0 μm is red) GLIMPSE images of the 10 high-quality PNe candidates from Parker et al. (2012), within the CORNISH survey region. All images are 25 arcsec × 25 arcsec in size and the CORNISH beam size is shown on the first image (A colour version of this figure is available in the online journal).

Downloaded from https://academic.oup.com/mnras/article-abstract/480/2/2423/5056229 by University of Leeds user on 14 November 2018

thermal free–free emission. The 2 per cent exhibiting non-thermal emission at a 3σ significance level are likely very young PNe.

– 22 out of the 76 CORNISH-PNe within the IPHAS survey region were found to have H α emitting counterparts. The PNe not detected by IPHAS are likely due to line-of-sight extinction.

– The broad distribution of the CORNISH-PNe in the MIR shows a sample dominated by different emission mechanisms across the different IRAC bands. This broad distribution is also observed in NIR colours.

– Some of the CORNISH-PNe, as expected, show higher reddening compared to previous PNe samples studied in the NIR.

– In the FIR, the CORNISH-PNe show a wider range of colours compared to the optically detected PNe studied by Anderson et al. (2012).

– We estimated extinction using the methods in Section 3.4. Extinction variations towards the CORNISH-PNe using the different methods reflect a sample dominated by different emission mechanisms across the NIR bands, hence, a possible range of intrinsic colours.

– Heliocentric distances were estimated using the Frew et al. (2016) calibration. The average distance for the CORNISH-PNe is 14 kpc with a corresponding average physical diameter of 0.14 pc.

– A catalogue of 169 CORNISH-PNe is presented. We find 90 new PNe, out of which 12 are newly discovered and 78 are newly classified as PN. A further 47 suspected PNe are confirmed as such from the analysis here and 24 known PNe were detected. Eight sources are classified as possible PNe or other source types.

– The clean sample of PNe, together with the extensive photometry and analysis presented here, should form good training sets in using machine learning to build classification/identification models for PNe in future large radio surveys.

ACKNOWLEDGEMENTS

The authors thank Filipovic, Miroslav for the thorough review and excellent suggestions and comments that have improved the quality of this paper. TI acknowledges OSAPND for funding through the award of a scholarship. This research made use of the NASA/IPAC Infrared Science Archive, which is operated by the Jet Propulsion Laboratory, California Institute of Technology, under contract with the National Aeronautics and Space Administration; data products from the SuperCOSMOS H-alpha Survey (SHS); the HASH PN data base at hashpn.space. This research also made use of the SIMBAD data base and the VizieR services, operated at CDS, Strasbourg, France, and SAOImage dS9, developed by the Smithsonian Astrophysical Observatory.

REFERENCES

Acker A., Marcout J., Ochsenbein F., Stenholm B., Tylenda R., Schohn C., 1992, The Strasbourg-ESO Catalogue of Galactic Planetary Nebulae. Parts I, II, European Southern Observatory , Garching (Germany)
Anderson L. D., Bania T. M., Balser D. S., Rood R. T., 2011, ApJS, 194, 32
Anderson L. D., Zavagno A., Barlow M. J., García-Lario P., Noriega-Crespo A., 2012, A&A, 537, A1
Anderson L. D., Armentrout W. P., Johnstone B. M., Bania T. M., Balser D. S., Wenger T. V., Cunningham V., 2015, ApJS, 221, 26
Anderson L. D. et al., 2017, A&A, 605, A58
Balick B., 1987, AJ, 94, 671
Barentsen G. et al., 2014, MNRAS, 444, 3230
Bear E., Soker N., 2017, ApJ, 837, L10
Becker R. H., White R. L., Helfand D. J., Zoonematkermani S., 1994, ApJS, 91, 347
Benjamin R. A. et al., 2003, PASP, 115, 953
Bietenholz M. F., Kassim N., Frail D. A., Perley R. A., Erickson W. C., Hajian A. R., 1997, ApJ, 490, 291
Bojičić I. S., Parker Q. A., Filipović M. D., Frew D. J., 2011, MNRAS, 412, 223
Bozzetto L. M. et al., 2017, ApJS, 230, 2
Cardelli J. A., Clayton G. C., Mathis J. S., 1989, ApJ, 345, 245
Carey S. J. et al., 2009, PASP, 121, 76
Caswell J. L., 2001, MNRAS, 326, 805
Cerrigone L., Hora J. L., Umana G., Trigilio C., 2009, ApJ, 703, 585
Cerrigone L., Trigilio C., Umana G., Buemi C. G., Leto P., 2011, MNRAS, 412, 1137
Cerrigone L., Umana G., Trigilio C., Leto P., Buemi C. S., Ingallinera A., 2017, MNRAS, 468, 3450
Chu Y.-H. et al., 2000, in Kastner J. H., Soker N., Rappaport S., eds, ASP Conf. Ser. Vol. 199, Asymmetrical Planetary Nebulae II: From Origins to Microstructures. Astron. Soc. Pac., San Francisco, p. 419
Churchwell E. et al., 2009, PASP, 121, 213
Claussen M. J., Goss W. M., Frail D. A., Seta M., 1999, AJ, 117, 1387
Cohen M. et al., 2007a, ApJ, 669, 343
Cohen M. et al., 2007b, ApJ, 669, 343
Cohen M., Parker Q. A., Green A. J., Miszalski B., Frew D., Murphy T., 2011, MNRAS, 413, 514
Condon J. J., Kaplan D. L., 1998, ApJS, 117, 361
Condon J. J., Cotton W. D., Greisen E. W., Yin Q. F., Perley R. A., Taylor G. B., Broderick J. J., 1998, AJ, 115, 1693
Condon J. J., Kaplan D. L., Terzian Y., 1999, ApJS, 123, 219
Cooper H. D. B. et al., 2013, MNRAS, 430, 1125
Corradi R. L. M. et al., 2008, A&A, 480, 409
Corradi R. L. M. et al., 2010, A&A, 509, A41
Cox N. L. J., García-Hernández D. A., García-Lario P., Manchado A., 2011, AJ, 141, 111
Cox N. L. J., Pilleri P., Berné O., Cernicharo J., Joblin C., 2016, MNRAS, 456, L89
De Marco O., 2009, PASP, 121, 316
De Marco O., Long J., Jacoby G. H., Hillwig T., Kronberger M., Howell S. B., Reindl N., Margheim S., 2015, MNRAS, 448, 3587
Drew J. E. et al., 2005, MNRAS, 362, 753
Ducati J. R., Bevilacqua C. M., Rembold S. B., Ribeiro D., 2001, ApJ, 558, 309
Felli M., Testi L., Schuller F., Omont A., 2002, A&A, 392, 971
Filipović M. D. et al., 2009, MNRAS, 399, 769
Fragkou V., Bojičić I., Frew D., Parker Q., 2017, in Liu X., Stanghellini L., Karakas A., eds, IAU Symp. Vol. 323, Planetary Nebulae: Multi-Wavelength Probes of Stellar and Galactic Evolution. p. 329, Cambridge University Press, Cambridge, UK, CB2 8BS
Freeman M. et al., 2014, ApJ, 794, 99
Frew D. J., Parker Q. A., 2010, PASA, 27, 129
Frew D. J., Parker Q. A., Bojičić I. S., 2016, MNRAS, 455, 1459
Gaensler B. M., Slane P. O., 2006, ARA&A, 44, 17
Garcia-Lario P. et al., 1997, A&AS, 126
García-Segura G., Langer N., Różyczka M., Franco J., 1999, ApJ, 517, 767
García-Segura G., López J. A., Franco J., 2005, ApJ, 618, 919
Gómez J. F., Rizzo J. R., Suárez O., Miranda L. F., Guerrero M. A., Ramos-Larios G., 2011, ApJ, 739, L14
Gonzalez O. A., Rejkuba M., Zoccali M., Valenti E., Minniti D., Schultheis M., Tobar R., Chen B., 2012, A&A, 543, A13
González-Solares E. A. et al., 2008, MNRAS, 388, 89
Griffin M. et al., 2009, in Pagani L., Gerin M., eds, EAS Publication Series: Astronomy in the Submillimeter and Far Infrared Domains with the Herschel Space Observatory, 34 p. 33, EDP Sciences
Gutermuth R. A., Heyer M., 2015, AJ, 149, 64
Guzman-Ramirez L., Lagadec E., Jones D., Zijlstra A. A., Gesicki K., 2014, MNRAS, 441, 364
Hands A. D. P., Warwick R. S., Watson M. G., Helfand D. J., 2004, MNRAS, 351, 31
Helfand D. J., Becker R. H., White R. L., Fallon A., Tuttle S., 2006, AJ, 131, 2525

Downloaded from https://academic.oup.com/mnras/article-abstract/480/2/2423/5056229 by University of Leeds user on 14 November 2018

Hoare M. G., 1990, MNRAS, 244, 193
Hoare M. G., 2002, in Crowther P., ed., ASP Conf. Ser. Vol. 267, Hot Star Workshop III: The Earliest Phases of Massive Star Birth. Astron. Soc. Pac., San Francisco, p. 137
Hoare M. G., Drew J. E., Muxlow T. B., Davis R. J., 1994, ApJ, 421, L51
Hoare M. G. et al., 2012, PASP, 124, 939 (Paper I)
Hora J. L., Latter W. B., Allen L. E., Marengo M., Deutsch L. K., Pipher J. L., 2004, ApJS, 154, 296
Indebetouw R. et al., 2005, ApJ, 619, 931
Kalcheva I. E., Hoare M. G., Urquhart J. S., Kurtz S., Lumsden S. L., Purcell C. R., Zijlstra A. A., 2018, A&A, 615, A103 (Paper III)
Kaler J. B., 1983, ApJ, 264, 594
Kanarek G., Shara M., Faherty J., Zurek D., Moffat A., 2015, MNRAS, 452, 2858
Kastner J. H., 2007, in Corradi R. L. M., Manchado A., Solur N., eds, Asymmetrical Planetary Nebulae IV, Instituto de Astrofisica de Canarias, La Palma, p. 5
Kastner J. H., Montez R., Jr., Balick B., De Marco O., 2008, ApJ, 672, 957
Kistiakowsky V., Helfand D. J., 1995, AJ, 110, 2225
Kohoutek L., 2001, A&A, 378, 843
Kronberger M., Jacoby G. H., Harmer D., Patchick D., 2014, in Asymmetrical Planetary Nebulae VI Conference. p. 47, Available at: http://www.astroscu.unam.mx/apn6/PROCEEDINGS/
Kwok S., 1982, ApJ, 258, 280
Kwok S., 1985, AJ, 90, 49
Kwok S., 1993, AcA, 43, 359
Kwok S., 2003, in Corradi R. L. M., Mikolajewska J., Mahoney T. J., eds, ASP Conf. Vol. 303, Symbiotic Stars Probing Stellar Evolution. Astron. Soc. Pac., San Francisco, p. 428
Kwok S., 2007, Asymmetrical Planetary Nebulae IV, Cambridge University Press , Cambridge, UK
Kwok S., 2010, PASA, 27, 174
Kwok S., Hrivnak B. J., Milone E. F., 1986, ApJ, 303, 451
Lakićević M. et al., 2015, ApJ, 799, 50
Leto P., Umana G., Trigilio C., Buemi C. S., Dolei S., Manzitto P., Cerrigone L., Siringo C., 2009, A&A, 507, 1467
Lucas P. W. et al., 2008, MNRAS, 391, 136
Lumsden S. L., Hoare M. G., Urquhart J. S., Oudmaijer R. D., Davies B., Mottram J. C., Cooper H. D. B., Moore T. J. T., 2013, ApJS, 208, 11
Mampaso A. et al., 2006, A&A, 458, 203
Marquez-Lugo R. A., Guerrero M. A., Ramos-Larios G., Miranda L. F., 2015, MNRAS, 453, 1888
Matsuura M., Zijlstra A. A., Gray M. D., Molster F. J., Waters L. B. F. M., 2005, MNRAS, 363, 628
Matsuura M., Indebetouw R., Kamenetzky J., McCray R., Zanardo G., Barlow M. J., Dwek E., 2015, in Iono D., Tatematsu K., Wootten A., Testi L., eds, ASP Conf. Ser. Vol. 499, Revolution in Astronomy with ALMA: The Third Year. Astron. Soc. Pac., San Francisco, p. 323
Miszalski B., Parker Q. A., Acker A., Birkby J. L., Frew D. J., Kovacevic A., 2008, MNRAS, 384, 525
Miszalski B., Mikołajewska J., Udalski A., 2013, MNRAS, 432, 3186
Moe M., De Marco O., 2006, ApJ, 650, 916
Molinari S. et al., 2010, PASP, 122, 314
Molinari S. et al., 2016, A&A, 591, A149
Oliveira J. M. et al., 2013, MNRAS, 428, 3001
Parker Q. A. et al., 2005, MNRAS, 362, 689
Parker Q. A. et al., 2006, MNRAS, 373, 79
Parker Q. A. et al., 2012, MNRAS, 427, 3016
Parker Q. A., Bojičić I., Frew D. J., 2017, in Liu X., Stanghellini L., Karakas A., eds, Proc. IAU Symp. 323, Planetary Nebulae: Multi-Wavelength Probes of Stellar and Galactic Evolution. Cambridge University Press, Cambridge, UK, p. 36
Pena M., Torres-Peimbert S., 1987, Rev. Mex. Astron. Astrofis, 14, 534
Pérez-Sánchez A. F., Vlemmings W. H. T., Tafoya D., Chapman J. M., 2013, MNRAS, 436, L79
Phillips J. P., 2003, A&A, 412, 791
Phillips J. P., Márquez-Lugo R. A., 2011, Rev. Mex. Astron. Astrofis., 47, 83
Phillips J. P., Ramos-Larios G., 2008, MNRAS, 386, 995
Phillips J. P., Ramos-Larios G., 2009, MNRAS, 396, 1915
Phillips J. P., Zepeda-Garcia D., 2009, MNRAS, 394, 1875
Pinheiro Gonçalves D., Noriega-Crespo A., Paladini R., Martin P. G., Carey S. J., 2011, AJ, 142, 47
Poglitsch A. et al., 2008, Proc.SPIE, 7010. p. 701005
Pottasch S. R., 1986, Comptes Rendus sur les Journees de Strasbourg, 8, 97
Pottasch S. R. et al., 1984, A&A, 138, 10
Pottasch S. R., Beintema D. A., Feibelman W. A., 2000, A&A, 363, 767
Preite-Martinez A., 1988, A&AS, 76, 317
Purcell C. R. et al., 2013, ApJS, 205, 1 (Paper II)
Ramos-Larios G., Phillips J. P., 2005, MNRAS, 357, 732
Ramos-Larios G., Guerrero M. A., Sabin L., Santamaría E., 2017, MNRAS, 470, 3707
Ratag M. A., Pottasch S. R., 1991, A&AS, 91, 481
Reach W. T. et al., 2005, PASP, 117, 978
Reach W. T. et al., 2006, AJ, 131, 1479
Ressler M. E., Cohen M., Wachter S., Hoard D. W., Mainzer A. K., Wright E. L., 2010, AJ, 140, 1882
Robitaille T. P. et al., 2008, AJ, 136, 2413
Rodríguez-Flores E. R., Corradi R. L. M., Mampaso A., García-Alvarez D., Munari U., Greimel R., Rubio-Díez M. M., Santander-García M., 2014, A&A, 567, A49
Rosen S. R. et al., 2016, A&A, 590, A1
Rosolowsky E. et al., 2010a, ApJS, 188, 123
Ruffle P. M. E., Zijlstra A. A., Walsh J. R., Gray M. D., Gesicki K., Minniti D., Comeron F., 2004, MNRAS, 353, 796
Sabin L. et al., 2014, MNRAS, 443, 3388
Sahai R., Trauger J. T., 1998, AJ, 116, 1357
Sahai R., Morris M., Sánchez Contreras C., Claussen M., 2007, AJ, 134, 2200
Sahai R., Morris M. R., Villar G. G., 2011, AJ, 141, 134
Siódmiak N., Tylenda R., 2001, A&A, 373, 1032
Stanghellini L., Shaw R. A., Villaver E., 2008, ApJ, 689, 194
Suarez O. et al., 2015, ApJ, 806, 105
Taylor A. R., Goss W. M., Coleman P. H., van Leeuwen J., Wallace B. J., 1996, ApJS, 107, 239
Tylenda R., Acker A., Stenholm B., Koeppen J., 1992, A&AS, 95, 337
Urquhart J. S. et al., 2009a, A&A, 501, 539
Urquhart J. S. et al., 2009b, A&A, 501, 539
Urquhart J. S. et al., 2013, MNRAS, 435, 400
Van de Steene, G. C., 2017, in Liu X., Stanghellini L., Karakas A., eds, Proc. IAU Symp. 323, Planetary Nebulae: Multi-Wavelength Probes of Stellar and Galactic Evolution. p. 128, 12, Cambridge University Press, Cambridge, UK
van de Steene G. C., Pottasch S. R., 1995, A&A, 299, 238
van de Steene G. C., Jacoby G. H., Pottasch S. R., 1996, A&AS, 118, 243
Van de Steene G. C. et al., 2015, A&A, 574, A134
van Hoof P. A. M., 2000, MNRAS, 314, 99
van Hoof P. A. M., Oudmaijer R. D., Waters L. B. F. M., 1997, MNRAS, 289, 371
Viironen K. et al., 2009b, A&A, 502, 113
Viironen K. et al., 2009, A&A, 504, 291
Villaver E., García-Segura G., Manchado A., 2002, ApJ, 571, 880
Weidmann W. A., Gamen R., van Hoof P. A. M., Zijlstra A., Minniti D., Volpe M. G., 2013, A&A, 552, A74
White R. L., Becker R. H., Helfand D. J., 2005, AJ, 130, 586
Whitelock P. A., 1985, MNRAS, 213, 59
Williams B. J., Temim T., 2016, Infrared Emission from Supernova Remnants: Formation and Destruction of Dust. Springer International Publishing, Switzerland. p. 1
Willner S. P., Becklin E. E., Visvanathan N., 1972, ApJ, 175, 699
Wood D. O. S., Churchwell E., 1989a, ApJS, 69, 831
Wood D. O. S., Churchwell E., 1989b, ApJ, 340, 265
Woodall J. M., Gray M. D., 2007, MNRAS, 378, L20
Wright E. L. et al., 2010, AJ, 140, 1868
Zijlstra A. A., 1990, A&A, 234, 387
Zijlstra A. A., Pottasch S. R., 1991, A&A, 243, 478

Downloaded from https://academic.oup.com/mnras/article-abstract/480/2/2423/5056229 by University of Leeds user on 14 November 2018

Zoonematkermani S., Helfand D. J., Becker R. H., White R. L., Perley R. A., 1990, ApJS, 74, 181
Wenger M., Ochsenbein F., Egret D., Dubois P., Bonnarel F., Borde S., Genova F., Jasniewicz G., Laloë S., Lesteven S., Monier R., 2000, A&AS, 143, 9

SUPPORTING INFORMATION

Supplementary data are available at *MNRAS* online.

Table A1. Radio properties of the CORNISH-PNe. For the angular sizes of sources whose deconvolved sizes could not be determined, we propagated an upper limit of 3σ and they are preceded by '$<$'. Column 8 shows measured (aperture photometry) 1.4 GHz flux densities (MAGPIS) not present in the point source catalogue.
Table A2. Measured NIR magnitudes and MIR flux densities for the CORNISH-PNe. These are measured using aperture photometry as described in Section 2.4. In the NIR, some of the CORNISH-PNe were not detected in one or more bands. For such sources, the corresponding columns are left blank. For non-detections in one or more of the bands and where the measured flux density is less than 3σ in the MIR, we have defined an upperlimit of 3σ limit preceded by '$<$'.
Table A3. Extinction table showing A_V from the different methods in Section 3.4 for all the CORNISH-PNe. Sources whose H α emission area is larger than radio, we have indicated using *.
Table A4. Distances and physical diameters estimated for the CORNISH-PNe. For the angular sizes whose deconvolved sizes could not be determined, we have stated the upper ($<$) and lower limits ($>$) for the distances and physical diameters, respectively.

Please note: Oxford University Press is not responsible for the content or functionality of any supporting materials supplied by the authors. Any queries (other than missing material) should be directed to the corresponding author for the article.

This paper has been typeset from a TEX/LATEX file prepared by the author.

Downloaded from https://academic.oup.com/mnras/article-abstract/480/2/2423/5056229 by University of Leeds user on 14 November 2018